Piezoelectric damping of a bladed rail

Design of passive and active damping for an aerospace structure

Donovan Maréchal

Master thesis submitted under the supervision of
Prof. Christophe Collette

the co-supervision of
Prof. Arnaud Deraemaeker

in order to be awarded the Degree of
Master of Science in Electromechanical Engineering
major in Mechatronics and Mechanical constructions

Academic year
2019 – 2020

ULB UNIVERSITÉ LIBRE DE BRUXELLES

ULB UNIVERSITÉ LIBRE DE BRUXELLES

Exemplaire à apposer sur le mémoire ou travail de fin d'études,
au verso de la première page de couverture.

Fait en deux exemplaires, **Bruxelles, le** 8/6/2020

Signature

Réservé au secrétariat :	**Mémoire réussi***	**OUI**
		NON

CONSULTATION DU MEMOIRE/TRAVAIL DE FIN D'ETUDES

Je soussigné

NOM : MARÉCHAL

PRENOM : DONOVAN

TITRE du travail : Piezoelectric damping of a bladed rail

AUTORISE*

~~**REFUSE***~~

la consultation du présent mémoire/travail de fin d'études par les utilisateurs des bibliothèques de l'Université libre de Bruxelles.

Si la consultation est autorisée, le soussigné concède par la présente à l'Université libre de Bruxelles, pour toute la durée légale de protection de l'œuvre, une licence gratuite et non exclusive de reproduction et de communication au public de son œuvre précisée ci-dessus, sur supports graphiques ou électroniques, afin d'en permettre la consultation par les utilisateurs des bibliothèques de l'ULB et d'autres institutions dans les limites du prêt inter-bibliothèques.

Title: Piezoelectric damping of a bladed rail

Author: Donovan Maréchal

Master of Science in Electromechanical Engineering – major in Mechatronics and Mechanical constructions

Academic year: 2019 – 2020

Abstract

In a context of ever growing demand and environmental requirements, aircrafts are subject to innovation. In order to improve their efficiency, the mass of their components, such as bladed disks, is reduced at the cost of high vibration stresses. This work studied the implementation of active and passive piezoelectric damping devices on a simplified version of the bladed disk: the bladed rail. To avoid interfering with the aerodynamic area around the blades, piezoelectric patches were placed on the bottom surface of the rail. The bladed rail, as any periodic structure, possesses groups of closely located natural frequencies, corresponding to families of modes. The objective of this project was to damp the first family. To that end, State Space models were generated using a 3D finite element model and the Structural Dynamics Toolbox in Matlab. Passive damping techniques - resistive and inductive piezoelectric shunts - as well as active techniques -integral and resonant collocated controllers - were then applied to the models. As a result, the vibrations of the blades were diminished. The resonant controller showed the best damping performance but poor stability robustness. Inductive shunting and integral control, exhibiting similar performance, presented advantages and disadvantages depending on the user's limiting factors. Finally, preliminary experiments on a 3D-printed prototype of the bladed rail were conducted, in order to corroborate the simulation model.

Keywords: blisk, bladed rail, active damping, piezoelectric shunt, MIMO control, collocated sensor and actuator

Preface

This master thesis comes as a conclusion of a six-year journey discovering the amazing world of sciences and engineering. It ends my double degree from the Université libre de Bruxelles (ULB) and Ecole polytechnique (in France).

ULB taught me the fundamentals of an engineer mindset, providing me tools for the critical thinking and problem solving. At the Ecole polytechnique, I learned the beauty of mathematical abstraction applied to sciences. It is where I discovered specifically my interest in vibrations and smart materials. It was later at the California Institute of Technology, in Chiara Daraio's laboratory, that I understood the extent of the domain of vibrations and waves. As a result, I decided to complete my master thesis in this field, in Christophe Collette's laboratory, the Precision Mechatronics Laboratory.

This eight-month labour addresses the control of smart structures using piezoelectric transducers. For further in-depth understanding of the subject, I suggest you have a look at the reference books I used for this thesis. In particular, you will certainly find very useful: *Piezoelectric transducers for vibration control and damping* of S.R. Moheimani (2006) and *Vibration control of active structures: an introduction* of A. Preumont (2011).

That being said, I hope you enjoy reading this thesis.

Acknowledgements

I would like to give a special thank to my supervisor Christophe Collette, who proposed the subject of this master thesis and who was always available for guidance and good advice. I am delighted to have done this work in his laboratory. I also thank Arnaud Deraemaeker, my co-supervisor, for his help during this project, in particular with SDT and piezoelectric modelling.

A *kheily mamnoon* to Ahmad Paknejad with whom I worked in strong collaboration to complete this project. I really wish him success in his PhD and his future activities.

I thank the PML researchers, in particular Cédric Dumoulin that helped us with the simulations. I also thank the ULB staff: Salvo for the surface smoothing, Michel Osée for the cable soldering.

I am of course very grateful to my reviewers that gave a bit of their time reading and understanding a thesis not always covering their specific expertise. Your input really levelled up the quality this work.

Finally, thanks to my family that supported me, helped me, throughout my studies and allowed me to get to the end of it. Merci, siempre os seré agradecido.

Table of Contents

List of Figures

List of Tables

List of Abbreviations

NPF	Negative Position Feedback
PPF	Positive Position Feedback

List of Symbols

$C(s)$	Controller	-
C_{stat}	Static capacitance	F
C	Capacitance	F
D_i	Electric displacement field vector	C/m^2
E_i	Electric field vector	V/m
F_i	Force applied on the tip of blade i	N
G_m	Gain margin	dB
H_∞	Supremum norm	-
K_i	Effective electromechanical coupling factor for mode i	
L	Inductance	H
P_m	Phase margin	deg
Q	Charge	C
R	Resistance	Ω
S_{ij}	Matrix of compliance coefficients	m^2/N
V_{ai}	Actuator patch voltage of pair i	V
V_{si}	Sensor patch voltage of pair i	V
V	Voltage	V
X_i	Tip displacement of blade i	m
Δp	Peak reduction	dB
Ω_i	i^{th} natural frequency of the set structure and piezoelectric transducer when the transducer is open-circuited	Hz
ϵ_i, γ_{kl}	Strain vector	m/m
μ_i	Modal mass	-
ν_i	Strain energy density	J/m^3
ω_i	i^{th} natural frequency of the set structure and piezoelectric transducer when the transducer is short-circuited	Hz
$\phi_i(x)$	Mode shape	-
ρ	Density	kg/m^3
σ_i, τ_{kl}	Stress vector	N/m^2
ξ_f, ω_f	Controller's parameters	-
ξ_i	Modal damping	-
ξ	Primary damping	-
d_{ij}	Matrix of piezoelectric strain constants	m/V
e_{ij}^{σ}	Matrix of permitivity coefficients measured when the material is not restrained	F/m

g	Controller gain	-
k_{ij}	Matrix of electromechanical coupling coefficients	-
s	Complex frequency (Laplace transform)	Hz
$u(x)$	Actuator input	-
$v(x)$	Sensor output	-
$z_i(t)$	Generalised displacements	-

Chapter 1
Introduction

Chapter summary Aerospace structures are expected to become efficient in terms of energy consumption. Designing lighter structures is a way to achieve this, but it comes at the cost of a low internal damping which leads to increased vibrations. It is the case of the blisk, an integrated bladed disk, an essential component of turbomachines. Since the intrinsic damping of this structure is very low, traditional damping devices are not applicable anymore. Piezoelectric materials, able to transduce energy between the mechanical and electrical domain, are advantageous candidates as they can easily be placed on existing structures to implement passive damping (with shunt circuits) or active damping (using the piezoelectrics as sensors and actuators). This study intends to employ piezoelectric technology in order to conceive vibration absorbers for a simplified version of the blisk: the bladed rail.

1.1 Damping of aerospace structures

Air transportation is facing a crucial dilemma: while the demand is endlessly growing, so are the environmental standards. The functional efficiency (i.e. ratio between aircraft performance and fuel consumption) of aerospace structures is being improved by introducing new techniques to decrease drag, complexity, number of parts, and weight. This result is achieved in various ways, such as the use of new materials, of lightweight structural design and of smart structures [9].

The weight improvements have come at the cost of a reduction of structural damping (around 0.01%), inducing large vibratory stresses. These unwanted vibrations have a negative impact on the aerodynamic efficiency of the structure and cause high-cycle fatigue that can reduce the structure lifetime to half [10]. Therefore, vibration reduction technologies are required for high performance and long lifespan in today's aeroengines.

Turbomachines are notably concerned by this issue. The device exchanges energy with a fluid using continuous flow and rotating blades. Aside from aircraft engines, they can be found in wind turbines.

In the case of aircrafts, the turbomachine works by letting air enter through the front inlet leading it to a compressor, which consists of several blades attached to a disk mounted on a shaft. These rotating blades compress the air, and subsequently increase the pressure. The air is then mixed with sprayed fuel in the combustion chambers where a spark starts a combustion reaction. As a result, the expanding hot gases produced by the combustion go through a turbine to create shaft power, and through a nozzle to generate thrust. This shaft power drives the compressor, drawing new air into the machine, thus closing the cycle [11], see Figure 1.1.

Bladed disks are essential components of compressors in turbomachines. Their vibration modes are mainly excited by aerodynamic loading acting on the blades. The flow field inside the engine is inherently unsteady, producing pressure variations, which are perceived by the spinning blades as time-varying forces [1]. It can provoke a resonant response, resulting in high vibrations. Other types of excitation can also engender forced vibration in

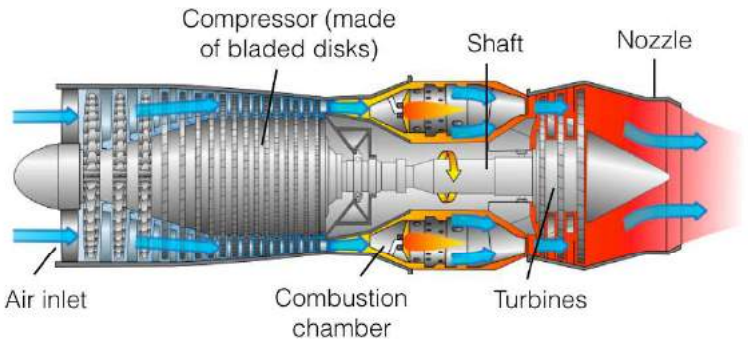

Figure 1.1 – Turbomachine representation - Image from wikimedia Commons File:Jet engine.svg at `https://commons.wikimedia.org/wiki/File:Jet_engine.svg`

a system mode: foreign object damage (for example a bird entering in contact with the turbomachine), nonlinearities caused by contact interfaces [12] or bladed disk mistuning [13].

In order to diminish vibrations in bladed disks, several techniques have been developed. The most classical one is the incorporation of friction devices. In conventional bladed disks, the disk and the blades are manufactured separately and then assembled, allowing to easily place those dampers at the root of the blade or between the blades themselves [1], see Figure 1.2. This method dissipates the energy by creating a contact surface between the vibrating parts.

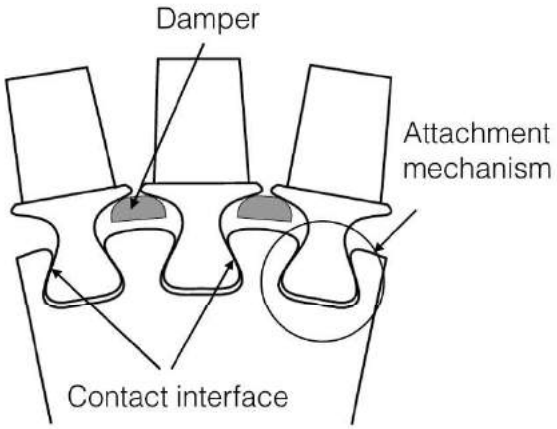

Figure 1.2 – Interface contact between the blade and the disk. Damping devices are placed in between [1].

Another approach consists in using viscoelastic materials associated to the structure [14]. Some materials can also be used as surface coating, improving the vibration reduction of the blades [15].

Contactless damping mechanism based on eddy current damping applied in bladed disk has been investigated, using permanent magnets and copper plates fixed on the blades [16]. This kind of solution is efficient, but difficult to implement.

As mentioned before, one of the priorities of the aerospace industry is to reduce the weight of aircraft parts, while improving their efficiency. This led to the creation of one part bladed disks, called blisks, see Figure 1.3 (a). Those new designs do not only make the structure lighter or reduce the number of parts; the elimination of the attachment mechanism between the blades and the disk induces the increase of the aerodynamic efficiency and the diminution of the blade drag. Besides, the interface of the blades and the disk is usually a point of crack initiation. By merging those parts, we get rid of that issue [17].

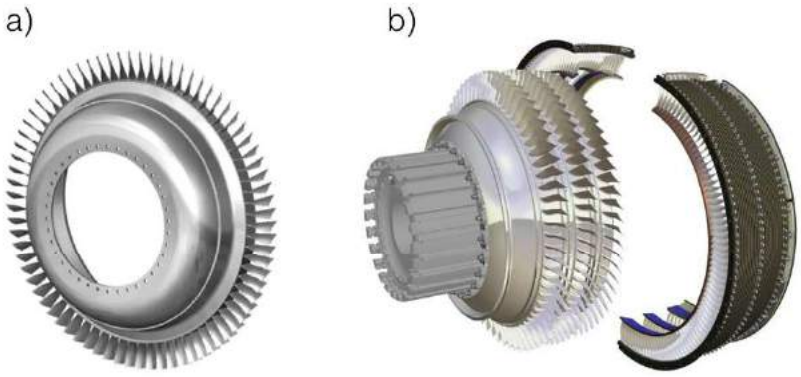

Figure 1.3 – (a) Blisk; (b) Turbine made of three bladed disks - the BluM [2]

However, this new design generates a new structural problem. Separated disk and blades possess frictional interface. But as a single part, the blisk exhibits little intrinsic damping. Moreover the classic damping devices that use friction or viscoelasticity are no more applicable considering there is no interface where to place them. This is precisely why other methods are needed.

In that context, the use of piezoelectric materials is more and more perceived as a serious easy-to-implement alternative application for blisk vibration damping.

1.2 Piezoelectic damping

1.2.1 Piezoelectric materials

The so-called piezoelectric effect was first discovered in 1880 by the brothers Pierre and Jacques Curie. They demonstrated that some materials are able to transform mechanical energy into electrical energy (direct piezoelectric effect). The converse piezoelectric effect, the creation of mechanical energy from electrical energy, was predicted one year later by Gabriel Lippmann [3].

Piezoelectricity, literally “electricity generated from pressure” in Greek, is found naturally in many monocrystalline materials, such as quartz, tourmaline, topaz and Rochelle salt. However those materials are usually not adapted for vibration reduction applications. Consequently artificial piezoelectric materials were developed out of polycrystalline ceramic materials, such as lead zirconate titanate (PZT), processed in order to exhibit piezoelectric properties. Easy to produce, they possess a strong electromechanical coupling [3].

Those ceramics are constituted of crystals, each of them composed of a small metal ion placed inside a lattice of larger metal ions and O_2, see Figure 1.4. Those elements are treated in order to be granted a remnant electrical polarisation. Mechanical compression or

tension on the element affects its dipole and creates a voltage: this is the direct piezoelectric effect. If a voltage is applied to the ceramic, the elements lengthens, known as the converse piezoelectric effect.

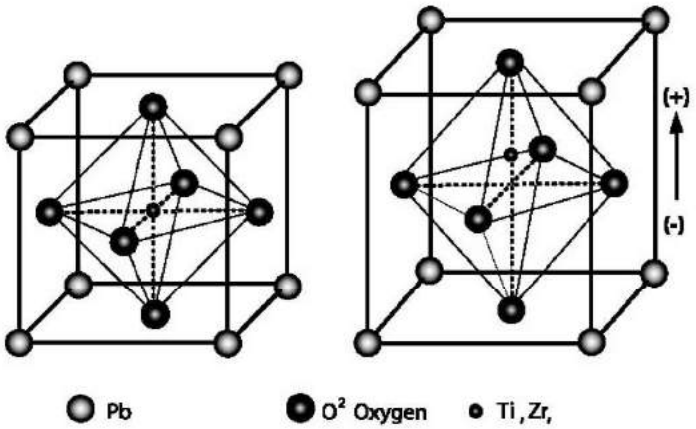

Figure 1.4 – Piezoelectric ceramic element before and after polarisation [3]. The "poling" process, applying a very high a strong, DC electric field, creates a permanent dipole.

At low drive, the piezoelectric ceramics can be considered as linear devices that transduce energy between the mechanical and electrical domains. They are called piezoelectric transducers. For higher drives, these materials exhibit non-linear effects, like hysteresis. Those effects can have an adverse influence on control stability and performance, and thus must sometimes be taken into account [3]. For what concerns us, we will assume that the piezoelectric transducers used in this project behave in a linear manner.

Piezoelectric constitutive equations That behaviour is modelled by a linear system of coupled equations [3]:

$$\begin{pmatrix} \epsilon_1 \\ \epsilon_2 \\ \epsilon_3 \\ \gamma_{23} \\ \gamma_{31} \\ \gamma_{12} \end{pmatrix} = \begin{bmatrix} S_{11} & S_{12} & S_{13} & S_{14} & S_{15} & S_{16} \\ S_{21} & S_{22} & S_{23} & S_{24} & S_{25} & S_{26} \\ S_{31} & S_{32} & S_{33} & S_{34} & S_{35} & S_{36} \\ S_{41} & S_{42} & S_{43} & S_{44} & S_{45} & S_{46} \\ S_{51} & S_{52} & S_{53} & S_{54} & S_{55} & S_{56} \\ S_{61} & S_{62} & S_{63} & S_{64} & S_{65} & S_{66} \end{bmatrix} \begin{pmatrix} \sigma_1 \\ \sigma_2 \\ \sigma_3 \\ \tau_{23} \\ \tau_{31} \\ \tau_{12} \end{pmatrix} + \begin{bmatrix} d_{11} & d_{21} & d_{31} \\ d_{12} & d_{22} & d_{32} \\ d_{13} & d_{23} & d_{33} \\ d_{14} & d_{24} & d_{34} \\ d_{15} & d_{25} & d_{35} \\ d_{16} & d_{26} & d_{36} \end{bmatrix} \begin{pmatrix} E_1 \\ E_2 \\ E_3 \end{pmatrix} \tag{1.1}$$

$$\begin{pmatrix} D_1 \\ D_2 \\ D_3 \end{pmatrix} = \begin{bmatrix} d_{11} & d_{12} & d_{13} & d_{14} & d_{15} & d_{16} \\ d_{21} & d_{22} & d_{23} & d_{24} & d_{25} & d_{26} \\ d_{31} & d_{32} & d_{33} & d_{34} & d_{35} & d_{36} \end{bmatrix} \begin{pmatrix} \sigma_1 \\ \sigma_2 \\ \sigma_3 \\ \tau_{23} \\ \tau_{31} \\ \tau_{12} \end{pmatrix} + \begin{bmatrix} e^{\sigma}_{11} & e^{\sigma}_{21} & e^{\sigma}_{31} \\ e^{\sigma}_{12} & e^{\sigma}_{22} & e^{\sigma}_{32} \\ e^{\sigma}_{13} & e^{\sigma}_{23} & e^{\sigma}_{33} \end{bmatrix} \begin{pmatrix} E_1 \\ E_2 \\ E_3 \end{pmatrix} \tag{1.2}$$

where:
σ_i, τ_{kl} correspond to the stress vector (N/m^2) - τ_{kl} being the shear stress;

ϵ_i, γ_{kl} correspond the strain vector (m/m) - γ_{kl} being the shear strain;
E_i is the electric field vector (V/m);
D_i is the electric displacement vector (C/m^2);
S_{ij} is the matrix of compliance coefficients (m^2/N);
e_{ij}^{σ} is the matrix of permitivity coefficients (F/m) - σ signifies that the permitivity is measured when the material is not restrained;
d_{ij} is the matrix of piezoelectric strain constants (m/V) - expression of the electromechanical coupling, it is defined as the ratio of developed free strain to the applied electric field.

Piezoelectric patch A huge advantage of piezoelectrics is that they are available in many shapes. A very common one - and the one we are interested in in this study - is the rectangular patch, see Figure 1.5. For this kind of device, the constitutive equations can be simplified as many terms of the constant matrices are brought to zero and some are equal. Assuming the patch is poled along the z axis (direction 3) and knowing that piezoelectric ceramics are transversely isotropic materials, we find that the terms that are equal are [3]:

$$\begin{gathered} S_{11} = S_{22} \\ S_{13} = S_{31} = S_{23} = S_{32} \\ S_{12} = S_{21} \\ S_{44} = S_{55} \\ S_{66} = 2(S_{11} - S_{12}) \\ d_{31} = d_{32} \\ d_{15} = d_{24} \\ e_{11}^{\sigma} = e_{22}^{\sigma} \end{gathered}$$

The constitutive equations can be rewritten:

$$\begin{pmatrix} \epsilon_1 \\ \epsilon_2 \\ \epsilon_3 \\ \gamma_{23} \\ \gamma_{31} \\ \gamma_{12} \end{pmatrix} = \begin{bmatrix} S_{11} & S_{12} & S_{13} & 0 & 0 & 0 \\ S_{12} & S_{11} & S_{13} & 0 & 0 & 0 \\ S_{13} & S_{13} & S_{33} & 0 & 0 & 0 \\ 0 & 0 & 0 & S_{44} & 0 & 0 \\ 0 & 0 & 0 & 0 & S_{44} & 0 \\ 0 & 0 & 0 & 0 & 0 & 2(S_{11} - S_{12}) \end{bmatrix} \begin{pmatrix} \sigma_1 \\ \sigma_2 \\ \sigma_3 \\ \tau_{23} \\ \tau_{31} \\ \tau_{12} \end{pmatrix} + \begin{bmatrix} 0 & 0 & d_{31} \\ 0 & 0 & d_{31} \\ 0 & 0 & d_{33} \\ 0 & d_{15} & 0 \\ d_{15} & 0 & 0 \\ 0 & 0 & 0 \end{bmatrix} \begin{pmatrix} E_1 \\ E_2 \\ E_3 \end{pmatrix} \tag{1.3}$$

$$\begin{pmatrix} D_1 \\ D_2 \\ D_3 \end{pmatrix} = \begin{bmatrix} 0 & 0 & 0 & 0 & d_{15} & 0 \\ 0 & 0 & 0 & d_{15} & 0 & 0 \\ d_{31} & d_{31} & d_{33} & 0 & 0 & 0 \end{bmatrix} \begin{pmatrix} \sigma_1 \\ \sigma_2 \\ \sigma_3 \\ \tau_{23} \\ \tau_{31} \\ \tau_{12} \end{pmatrix} + \begin{bmatrix} e_{11}^{\sigma} & 0 & 0 \\ 0 & e_{11}^{\sigma} & 0 \\ 0 & 0 & e_{33}^{\sigma} \end{bmatrix} \begin{pmatrix} E_1 \\ E_2 \\ E_3 \end{pmatrix} \tag{1.4}$$

The piezoelectric strain constants are related to different deformations of the patch: d_{33} is linked to a compression/extension along the thickness of the patch, d_{31} corresponds

to the bending of the patch and d_{15} to the patch in shear.

Thin patches are bonded to structure surfaces and used in bending (working with d_{31} coefficient). For compression/extension (d_{33}) other configurations of piezoelectrics are adopted: stacks.

We see that modelling the behaviour of a ceramic piezoelectric patch only requires to know a total of nine values, depending on the kind of piezoelectric used.

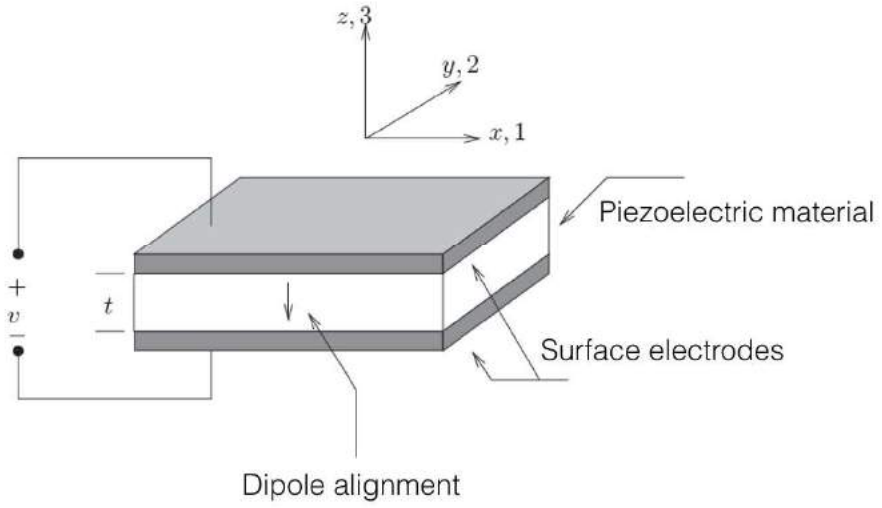

Figure 1.5 – Piezoelectric patch with polarisation in direction 3 [3]

1.2.2 Application to vibration reduction

Piezoelectrics are widely used in vibration damping applications due to their high electromechanical coupling coefficient that allows excellent actuation and sensing abilities. Their non-intrusive nature is a huge advantage as they can be embedded on structures without having to modify them and without adding much mass. They also function in a large frequency bandwidth and their cost is relatively low [18] [3].

Damping strategies based on piezoelectric materials can as well be active or passive, whether they require external energy or not. Passive techniques are always stable and are simple to design, while active ones give better results but are more difficult to implement because of the complex electronics they require.

Passive techniques associate piezoelectrics with a shunt circuit (i.e. circuit composed of a resistance with sometimes an inductance and a capacitance). The mechanical energy from the vibrations is transduced to electrical energy that is eventually dissipated in the resistance in the form of heat. Piezoelectric shunts are used in many areas, such as: noise control, vibration control of hard drives, sound transmission suppression, machining, railway vehicles and of course turbomachinery components [19][20].

In active damping methods, piezoelectrics act as actuators and sensors in order to establish a feedback loop, requiring an external power source. The actuator can be used as sensor at the time, which is called self-sensing. There are many applications for those methods, for example: in large space structures, space-trusses vibration reduction; in civil structures, applied to building frames; helicopter's rotor blade vibration control; in aircrafts, control of the flutter of the wings of the planes, and the buffeting of the tail [18].

Hybrid approaches that combine passive and active damping also exist and allow better performance than passive damping while using less energy than purely active damping [21].

A growing attention is given to piezoelectric energy harvesting [22]. The technique intends to benefit from the electrical energy generated by the piezoelectric material. For vibration control, that energy can be used as a supply for active control, and therefore make it more energy efficient [23]. Energy harvesting is promising also outside of the vibration control field, used as wearable objects that could power both portable electronics and biomedical devices. It also allows the creation of new self-powered wireless sensors and systems [24].

In this study, we only focus on the implementation of passive and active damping, leaving to future works the use of hybrid techniques and energy harvesting.

1.3 MAVERIC project

This work takes part in a bigger project: the MAVERIC project. Its main objective is to design a new vibration absorber that is efficient, combining hybrid control and nonlinear vibration reduction; smart, in terms of electrical components; and applicable to industrial products, with a special focus on the aerospace sector. The laboratory investigates the use of piezoelectric patches to damp blisk structures. At the final step of the project, the absorber designs will be tested on a blisk provided by an industrial partner: Safran Aero Boosters.

To reduce the weight of their compressor, Safran Aero Boosters developed their own model of blisk: the BluM (Bladed Drum - See Figure 1.3 (b)). As mentioned before, blisks have little inherent damping and need the implementation of vibration reduction strategies. The damping method Safran is working on is based on the use of friction devices: friction rings embedded in the structure (system studied in [25]). The dimensioning of this solution is complicated and it exhibits a poor performance. In that context, MAVERIC researchers intend to apply their piezoelectric absorber to the BluM and demonstrate it shows better results than the friction devices.

The technology has much wider applications than aerospace, as it could be applied to almost any industrial sector where vibration and weight are an issue.

1.4 Bladed rail

The use of piezoelectric technology in turbines has been studied during the last decade. Many of those studies propose to place the piezoelectric patches directly on the blades of the turbomachinery components (as in [17]), as it is where the structure deforms the most. However, even if the results are positive in laboratory conditions, this configuration is difficult to apply to real systems. The patches on the blades can interfere with the flow and thus affect the aerodynamics efficiency of the structure. Besides piezoelectric components subject to such a flow could suffer from erosion.

This research focuses on a Bladed Rail, a simplified version of the blisk (see Figure 1.6). While the BluM is made of seventy-six blades, this structure is only composed of five blades on a straight support, reducing the complexity of the problem. It also considerably decreases the cost of the prototype, as it requires less material and a lower number of damping devices (piezoelectric patches).

Similar study has been done by B. Mokrani (2015), in his PhD thesis, where he suggested to place shunted patches on the bottom surface of the rail [2] and presented convincing results. His bladed rail is different from this one as it possesses other dimensions and support shape.

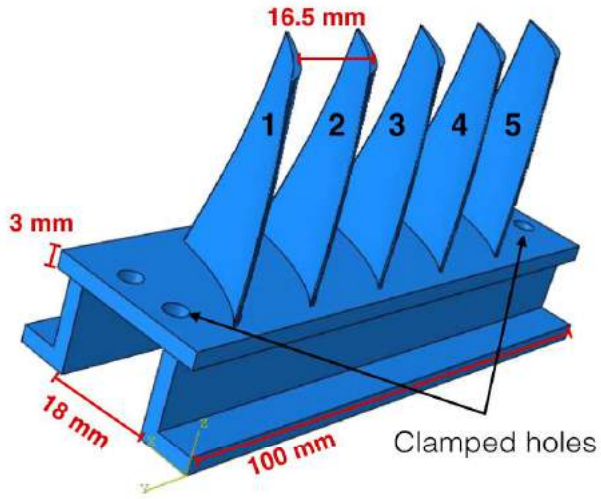

Figure 1.6 – Bladed Rail 3D model with some quotations - the support is clamped at the four extremity holes.

Real bladed disks are not only submitted to vibrations but also to high pressure and temperature constraints. This explains why titanium is widely used in the aerospace industry for its very good mechanical properties and its light weight. The present project however only focuses on the vibration response, which remains mostly unchanged when the structure is made of another metal (details in Appendix A). This is why we choose a cheaper and easier to manufacture material for the bladed rail: Steel.

The objective of the project is to damp the modes of the Bladed Rail related to the motion of the blades by placing the patches on the bottom surface, so that the aerodynamically active zone of the structure, which is located around the blades, is not disturbed. The patches placement problem is addressed in the next chapters.

Mokrani (2015) used shunted piezoelectric patches on the Bladed Rail. This current study aims to make a step further, improving the performances adopting active damping strategies. To do so, the results of active damping strategies will be developed and compared with the piezoelectric shunt.

Most of this work is numerical. The bladed rail is modelled with 3D finite elements and considered clamped at the two extremities of the support, see Figure 1.6. The first step of the project is to simulate the dynamics of the structure to understand where to place the piezoelectric patches. Then a reduced state-space model is extracted using the Structural Dynamics Toolbox on Matlab. The piezoelectric shunt employing five patches on the bottom surface is implemented and the results are evaluated. At that point, there is a passive damping reference and active methods, with five pairs of actuator-sensor piezoelectric patches, are developed. Those strategies are finally compared, evaluating damping performance and stability robustness.

An experimental prototype was 3D-printed so that the model is adapted to reality, and the control strategies reshaped in consequence. First results are presented but new

experiments should be carried out in future works to complete them.

Chapter 2
Bladed rail dynamics

Chapter summary The dynamics of the system is investigated in order to extract the resonance frequencies and the corresponding mode shapes. As the bladed rail is a periodic structure, the blade motion modes are organised in families in which the modes possess very close natural frequencies. This study will focus on damping the first family. The mode shapes are plotted, highlighting the coupling between the support bottom surface and the blades. Finally we see that the strain energy density map on the bottom surface of the bladed rail exhibits maximums in the areas under each blade. Those maximums are optimal locations for piezoelectric patches applied to vibration reduction.

2.1 Introduction

Although the bladed rail is a monolithic structure, it can be considered as a combination of two substructures: the support (or the rail) and the blades. The blades dynamics are linked to the rigidity of the support. If it was fully rigid, every blade would be a completely independent system with all the same resonance frequencies. However, as the rail is flexible, everything is connected and the dynamics of the structure is more complex, leading to several natural frequencies and modes.

The main objective of damping is to decrease the effect of resonances to avoid high vibration amplitudes. As it will be explained in following chapters (Chapters 3 and 4), the damping methods can be designed to act whether broadband or on targeted frequencies (said resonant). For the implementation of those resonant techniques, it is essential to previously know the natural frequencies of the structure.

The shapes of the specific modes we seek to target is another valuable information. The piezoelectric patches should be placed where they have more influence on the vibrations, which corresponds to the location of high strain energy. The electromechanical coupling factor of the piezoelectric measures its influence on each mode [26]. It is directly proportional to the modal strain energy density (detailed in Chapter 3). This is why the patches should be placed where the modal strain density is maximum.

As mentioned before, in this project, we aim to damp the blades by operating on the support. In order to understand how to achieve this, it is necessary to characterise the coupling between the support and the blades. To that end, the natural frequencies are first computed from simulation. Then relevant mode shapes are analysed, with a focus on the bottom surface of the support.

2.2 Method

Linear perturbation simulations with clamped boundary conditions are carried out on Abaqus in order to compute the twenty first natural frequencies and mode shapes. The model assumes that the rail is made out of an homogeneous and isotropic material with the theoretical mechanical properties of Steel, see Table 2.1:
The finite element analysis uses quadratic tetrahedral elements of size 2 mm, leading to a

Density (kg/m^3)	Young Modulus (MPa)	Poisson Coefficient
7800	200000	0.30

Table 2.1 – Steel mechanical properties [4]

model with 36629 elements. The mesh is shown on Figure 2.1. To corroborate the validity of that choice, a convergence study has been fulfilled and presented on Figure 2.2.

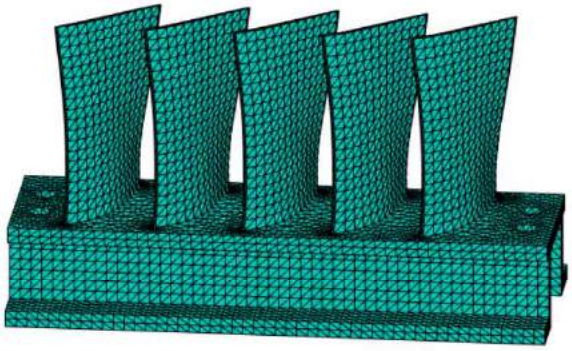

Figure 2.1 – Meshed blade rail with tetrahedral elements of size 2 mm

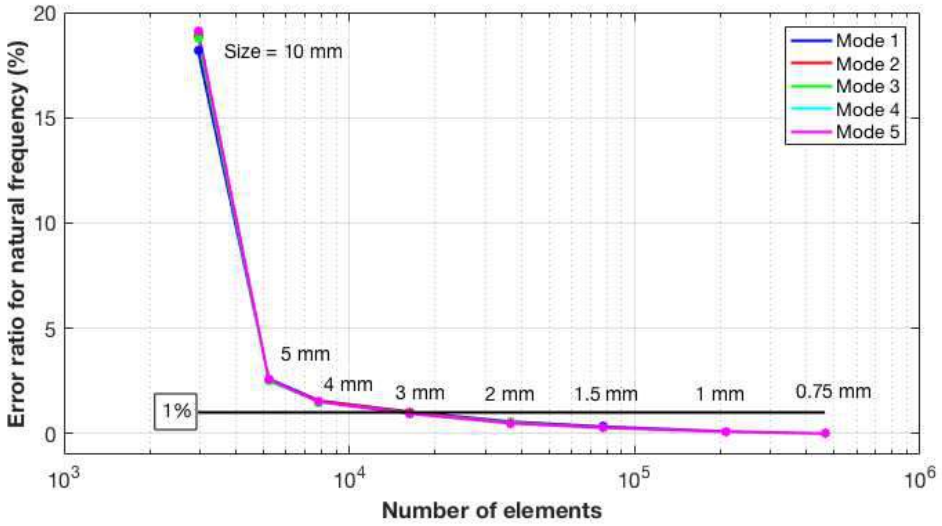

Figure 2.2 – Convergence study based on the natural frequencies. To check the validity of the mesh, the five first natural frequencies were computed for different sizes of elements and then compared to the frequencies obtained with the smallest size. Are considered acceptable mesh sizes the ones that have a deviation from the finest mesh of less than 1%: on the plot, the meshes with element size smaller than 3 mm. In an intent to lessen computational time consumption, we choose the mesh requiring fewer elements within that limit: the one with element size of 2 mm.

2.3 Natural frequencies and mode shapes

2.3.1 Mode families

The natural frequencies obtained by the simulation are plotted in function of their mode number on Figure 2.3. We can observe that some modes possess very close natural frequencies - those modes belong to the same "family" - while others are located in the gap between those families - they correspond to the support modes. This behaviour is typical of periodic structures such as the bladed rail.

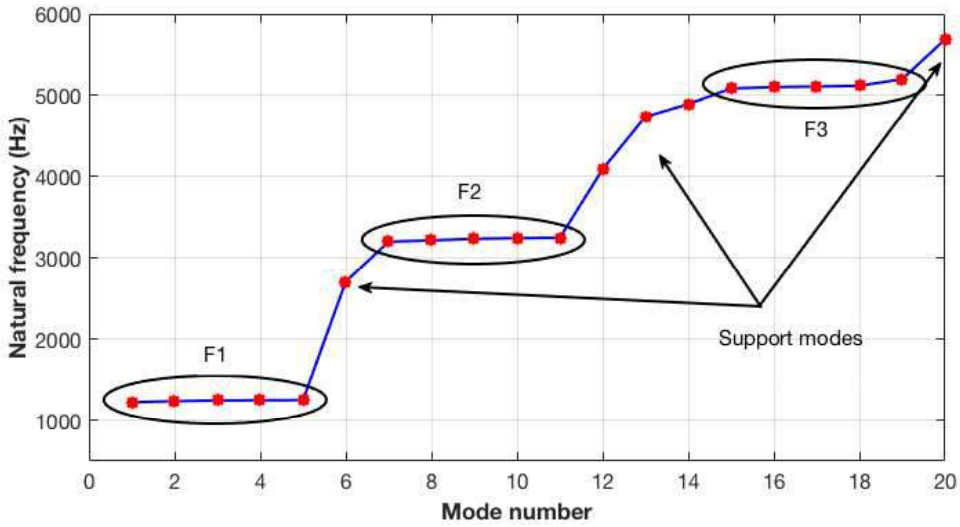

Figure 2.3 – Bladed rail natural frequencies. The ovals point out the mode families corresponding to the blade motions. The other modes are related to the support. The natural frequencies of the first family are 1237.3Hz, 1251.0Hz, 1259.2Hz, 1262.9Hz and 1264.6Hz, thus located in an range of 30 Hz.

The families correspond to bending or torsion modes of the blades. Modes of the first family are combinations of blades in their first bending mode moving in phase or out of phase. The next families are correlated to next blade modes of bending and torsion.

As mentioned before, if the support was completely rigid, each blade would be independent from the other, and logically the modes of the structure, which, for the first family, would still be a combination of bending blades in phase or out phase, would have the same frequency. Generally stiffer is the support, closer are the resonance frequencies of one family.

In order to reduce the complexity of the problem, our damping system design will only focus on the first family of modes. Damping the lower frequencies consists in a first step - and sometimes a sufficient one - in terms of improving vibration reduction.

2.3.2 Family 1 mode shapes

The mode shapes of the first family are shown in Figure 2.4. Those modes correspond as expected to a combination of the blades first bending mode. Depending on the mode, some blades have a strong displacement while others almost do not move.

To understand how to damp the blades motion from the bottom surface, the displacement field on that surface is plotted on Figure 2.5. Only the z direction of the displacement

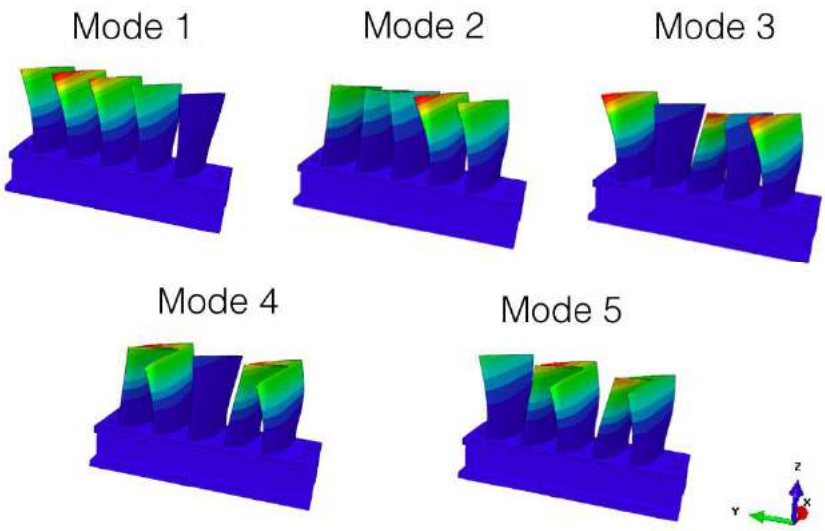

Figure 2.4 – Mode shapes of the first family modes. Red coloured areas are areas with maximum displacements - dark blue areas, minimum displacements.

is shown because it is what will mainly define the response of a piezoelectric patch in bending attached to the surface.

Comparing both Figures 2.4 and 2.5 one can clearly see the coupling between the support and blades motion: a high displacement of a blade causes higher displacement of the bottom surface under the blade while a still blade implies no displacement under it on the bottom surface. These observations highlight the fact that there is a possibility to act on the blades operating on the bottom surface, as those subsystems are directly connected.

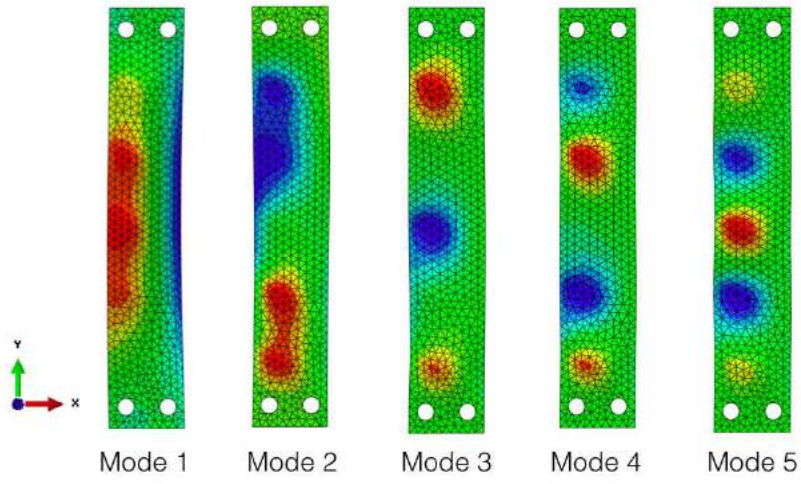

Figure 2.5 – Displacement field on the bottom surface for each mode in z direction (perpendicular to the surface). Red coloured areas are areas with maximum displacements - dark blue areas, maximum displacements of opposite phase. Green areas correspond to minimum amplitude displacement.

The more adequate location for piezoelectric patches on a structure is where their electromechanical coupling is maximised - in this case where the strain energy density is maximised on the bottom surface. The map of the strain energy density is displayed on Figure 2.6. It appears that for the five modes, the maximums are situated in the areas under the blades.

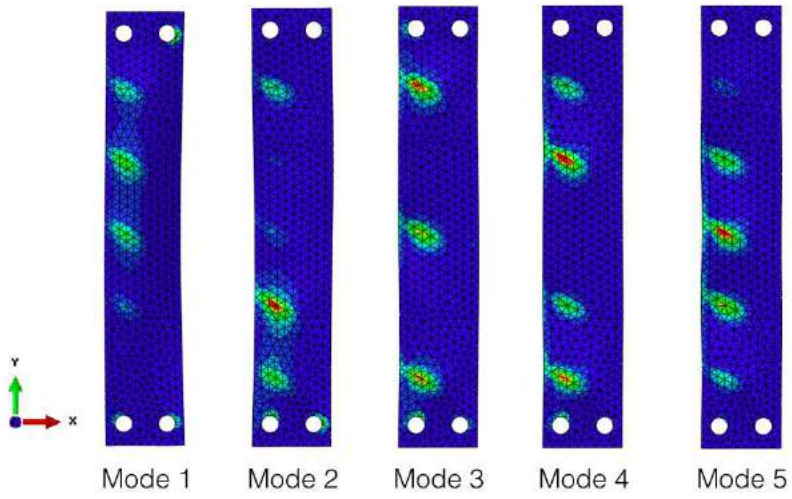

Figure 2.6 – Strain energy density field on the bottom surface for each mode. Red coloured areas are areas with maximum density - dark blue areas, minimum density.

2.4 Conclusion

The modes of the bladed rail can be classified in families of modes, related to the blades displacements and support modes. This study focuses on damping the modes of the first family.

The coupling between the bottom surface and the blades displacement is clearly visible, which confirms the possibility to act on the blades operating from the bottom surface.

The strain energy density map on the bottom surface shows maximums under the blades. This indicates that those areas are the best locations to install piezoelectric patches. This information allows to start designing the piezoelectric damping strategies.

Chapter 3

Passive damping

Chapter summary Passive damping with piezoelectric shunt consists in dissipating the vibration energy, transduced to electrical power, through a resistance in the form of heat. Three types of shunts are developed and applied to the bladed rail model, on which five patches have been added on the bottom surface under each blade. The purely resistive shunt allows a broadband vibration reduction, but is less effective than resonant inductive shunts to specifically damp the first family of modes. Two methods to tune the inductive shunts are proposed: the mean shunt approach, already studied in Mokrani's thesis (2015, [2]), and an H_∞ (supremum norm) optimisation approach.

3.1 Introduction

Passive damping techniques do not require external power to reduce vibrations in a structure. Hence their stability is guaranteed. They are based on dissipative phenomena that occur in friction, in viscoelesticity or also in hydrodynamics [27].

Piezoelectric passive absorbers, for their part, exploit electrical energy dissipation, connecting the vibrating piezoelectric device to a resistive shunt. The mechanical energy of the structure, transduced into electrical power, is liberated outside of the system in the form of heat.

In order to damp particular modes, the shunt circuit can be made resonant by including an inductance. As a piezoelectric is electrically a capacitance - linear relation between voltage and charge - the shunt becomes an oscillating RLC circuit. The electrical frequency of the circuit can then be tuned on the natural frequency of the structure in order to efficiently damp it.

The implementation of such devices on the BluM and the bladed rail have been studied by Mokrani (2015) in his PhD Thesis [2]. He proposes to place piezoelectric patches under the blades and develops a method to easily tune the shunt circuit for close natural frequencies: the mean shunt approach.

In this study, the damping effects of purely-resistive and resonant shunts on the bladed rail model are evaluated. The H_∞ optimisation which consists in minimising the maximum of a performance index is used to tune the parameters of shunt circuits. To assess the performance of the designed control system, obtained results are compared to that of the mean shunt [2].

Throughout this chapter, the concept of piezoelectric shunt are explained, describing the basic physics and modelling formulations. The three shunt circuit tunings used in this work are then presented. Subsequently, the simulations procedure and results are discussed.

3.2 Piezoelectric shunt

3.2.1 Piezoelectric transducer capacitance and coupling factor

A piezoelectric transducer, in the point of view of electrical components, is a capacitor, as it stores electrical energy in an electric field. In Eq. 1.2, one can see the linear relation between the electric displacement field $\vec{D}$ and the electric field $\vec{E}$. According to electrodynamics laws, the voltage applied on the transducer V and the free charge accumulated Q can be calculated by integrating those fields:

$$Q = \oint_A \vec{D}\, d\vec{\sigma} \tag{3.1}$$

$$V = \int_\Gamma \vec{E}\, d\vec{l} \tag{3.2}$$

where A is the closed surface of a small rectangular box mounted on one plate of the capacitor (electrode of the piezoelectric transducer);
$d\vec{\sigma}$ is the infinitesimal surface;
Γ is a path starting on one plate of the capacitor and ending on the other;
$d\vec{l}$ is the infinitesimal length.

From those relations, the capacitance Q/V can be deduced. In [26], its formula has been derived in the frequency domain for a piezoelectric transducer attached to a vibrating structure. For an undamped structure, we get (see expression amplitude plotted in Fig. 3.1):

$$\frac{Q}{V} = C_{stat} \frac{\prod_i 1 + \frac{s^2}{\Omega_i^2}}{\prod_j 1 + \frac{s^2}{\omega_j^2}} \tag{3.3}$$

where C_{stat} is the capacitance when the structure does not vibrate (i.e. static capacitance);
Ω_i is the i^{th} natural frequency of the set structure and piezoelectric transducer when the transducer is open-circuited (when $Q = 0$);
ω_j is the j^{th} natural frequency of the set structure and piezoelectric transducer when the transducer is short-circuited (when $V = 0$).

The natural frequencies of the global structure (primary structure and piezoelectric transducer) exhibit slight variations depending on the voltage applied on the transducer because it changes the stiffness of the overall structure. When the piezoelectric is open-circuited, the force needed to produce a strain is bigger than when it is short-circuited because part of the input energy is used to establish an electric field. In the short-circuited case, all the input energy goes to the deformation. If the force needed to deform a structure is increased, it means the stiffness augmented and that the natural frequencies are higher. It explains why $\Omega_k > \omega_k$ (k is the mode number), even if they are still very close.

Equation 3.3 indicates that a piezoelectric transducer behaves like a capacitor with varying capacitance, changing with the frequency of the structure it is attached to. Its amplitude changes a lot when the frequency is close to a structure resonance. In that case, the capacitance transfer function shows strong amplitude variations - a pole and a zero.

Piezoelectric transducers are characterised by an electromechanical coupling coefficient k_{mn} expressed as a ratio between the constants of Eq. 1.1 and 1.2 [3]:

$$k_{mn}^2 = \frac{d_{mn}^2}{S_{mn} e_{mn}^\sigma} \tag{3.4}$$

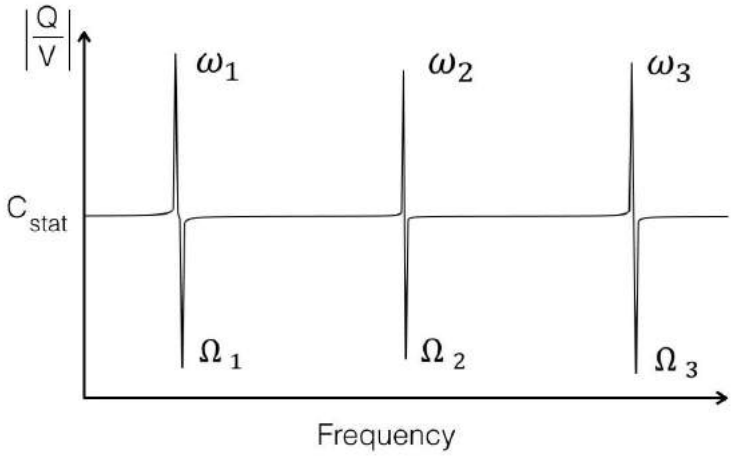

Figure 3.1 – Q/V transfer function for a piezoelectric transducer. The poles correspond to the natural frequency of the structure when the transducer is short-circuited and the zeros correspond to the natural frequency of the structure when open-circuited. At frequency zero, $Q/V = C_{stat}$, the static capacitance.

The higher the value of the coefficient is, the stronger is the influence of the piezoelectric device on the structure. For piezoelectric patches used in bending, as it is the case in this study, the coupling is mainly defined by $k_{13} = k$. k_{15} and k_{33} correspond respectively to piezoelectric patches employed in shear and in compression/extension.

To measure the influence of a patch over a specific mode, we employ the effective electromechanical coupling factor for mode i, K_i, calculated as a fraction involving the electromechanical coupling coefficient k and the strain energy density covered by the patch for mode i, ν_i:

$$K_i^2 = \frac{k^2 \nu_i}{1 - k^2} \tag{3.5}$$

This relation was mentioned in the previous chapter to justify why the optimal placement of the piezoelectric patches is in the area under the blades, as it is where the modal strain energy density is maximum. Indeed, Eq. 3.5 suggests that maximising the strain energy density covered by the patches for some particular modes maximises the influence of the transducer on the structure for those modes.

Another way to evaluate the influence of a piezoelectric device on a structure is looking at the difference between Ω_i and ω_i. If the natural frequencies of the overall structure varies a lot with the electrical constraints on the attached piezoelectric transducer (open-circuited or short-cicuited), it means that the electrical condition of the transducer considerably affects the mechanics of the structure, and thus it shows a high authority on its dynamics. In [26], an approximation of the effective electromechanical coupling factor is derived using those frequencies:

$$K_i^2 = \frac{k^2 \nu_i}{1 - k^2} \approx \frac{\Omega_i^2 - \omega_i^2}{\omega_i^2} \tag{3.6}$$

This equation implies that increasing the authority of the patches on a mode comes with enlarging the distance between the pole and the zero of the same mode in the capacitance transfer function Q/V.

3.2.2 Piezoelectric shunt circuits

Connecting a resistance path for electrical current on a piezoelectric transducer is known as piezoelectric shunting. It allows to reduce the vibrations of the host structure by energy dissipation through the shunt in the form of heat (Joule effect).

Resistive shunting The piezoelectric resistive shunt is schematised of Figure 3.2 (a). According to Kirchhoff's law, the voltage difference at the branches of the transducer is equal to the voltage difference through the resistance $V_R = RI$:

$$V_{piezo} = V = -RI = -sQR \tag{3.7}$$

$$\iff \left(\frac{Q}{V}\right)_{piezo} = -\frac{1}{sR} \tag{3.8}$$

in which Q/V is known or can be measured (see Figure 3.1).

Eq. 3.8 can be modelled closing a loop on the system between the output Q and the input V (Figure 3.2 (c)). The new system then represents the structure where a piezoelectric shunt mounted on it.

The R-shunt possesses the ability to damp multi-mode resonances. This is interesting for applications where all the modes are to be damped without distinction. When the objective is to target a specific frequency, it is possible to improve performance by using resonant shunts.

Inductive shunting Adding an inductance to the shunt results in an RLC circuit (see Figure 3.2 (b)). Those kinds of circuit possess oscillating properties and exhibit resonances. The circuit in Fig. 3.2 (b) is a one degree of freedom oscillating system, with one natural frequency ω_c:

$$\omega_c = \frac{1}{\sqrt{LC}} \tag{3.9}$$

where C is the capacitance of the piezoelectric transducer.

If the electrical natural frequency of the shunt is set on the targeted vibration mode frequency, the circuit will enter in resonance at the same time as the structure, and the current will reach very high amplitudes, which will lead to extensive dissipation through the resistance by Joule effect (dissipation power $P = RI^2$).

The Kirchhoff's law can again be applied. As the electric potential difference of an inductance is equal to $V_L = LsI$, we get:

$$V_{piezo} + V_R + V_L = V_{piezo} + RI + sLI = 0 \tag{3.10}$$

$$\iff \left(\frac{I}{V}\right)_{piezo} = -\frac{1}{R + sL} \iff \left(\frac{Q}{V}\right)_{piezo} = -\frac{1}{sR + s^2L} \tag{3.11}$$

In the same way as for the R-shunt, the inductive shunting of a structure can be modelled with a closed loop (see Figure 3.2 (d)).

RL-shunts are efficient to damp specific single modes, as well as closely located multi-modal resonances (such as resonances found in a family). However, it makes them sensitive to circuit mistuning. If the electrical frequency is not accurately set, the damping performance of such devices considerably decreases.

Many other categories of shunt circuits exist in the literature using passive but also

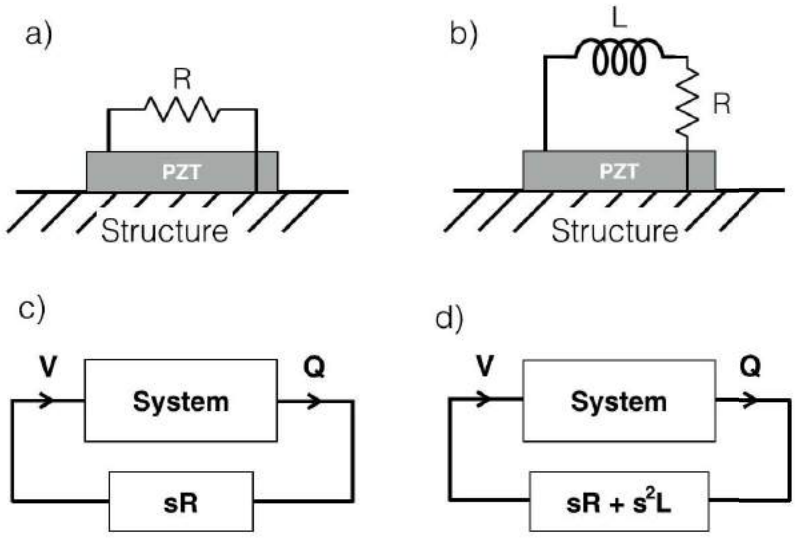

Figure 3.2 – (a) Illustration of an R-shunt circuit connected to a piezoelectric transducer (PZT); (b) illustration of an RL-shunt circuit connected to a PZT; (c) system transposition of an R-shunted piezoelectric transducer, closing a loop between the charge output Q and the voltage input V; (d) system transposition of an RL-shunted piezoelectric transducer.

active components. Some are based on nonlinear elements, switches, varying resistances; others are adapted to multimodes, creating multibranch circuits; some shunting components can be online tuned; etc. In his article [20], Marakakis (2019) proposes a review of those different techniques. In this work however, we only study the damping performances of passive linear shunts tuned on a single frequency.

3.2.3 Mean shunt approach

Although, in the case of the bladed rail, the objective is to damp five modes, their frequencies are very close. Parallel inductive shunts tuned on the different modes could be an option, but they are complicated to design because of the proximity of the resonances that implies strong interactions between the multiple circuit branches.

In [2], it is suggested to use a one-branch inductive circuit for all five modes, tuned on their average frequency $\overline{\omega}$. The concept allows to still effectively damp the modes while only needing a one loop shunt.

This proposition also consisted in placing identical piezoelectric patches under each blade, justified by the strain energy density maximums. The idea was therefore to shunt each one of those patches with identically tuned inductive circuits.

The values of the shunt components were chosen with the following equations:

$$L = \frac{1}{\overline{\omega}^2 C_{stat}} \tag{3.12}$$

$$R = \frac{2\hat{K}}{\overline{\omega} C_{stat}} \tag{3.13}$$

where $\hat{K}$ is defined as the overall effective electromechanical coupling factor:

$$\hat{K}^2 = \sum_{j=1}^{p} \overline{K}_j^2 \tag{3.14}$$

$$\overline{K}_j^2 = \frac{1}{N} \sum_{i=1}^{N} K_{ij}^2 \tag{3.15}$$

where N is the number of modes, p is the number of patches;
K_{ij} is the effective electromechanical coupling factor for the patch j on the mode i calculated using Eq. 3.6 with Ω_{ij}, the natural frequency of mode i of the structure detected by patch j when open-ciruited, and ω_i, the short-circuited the natural frequency of mode i of the structure when the patches are short-circuited (it does not depend on the patch).

K_{ij} essentially translates the influence of a patch to damp a mode. It is possible to deduce from their values that three patches, located under blade 1, 3 and 5 (see Figure 1.6), are sufficient to operate on the first family of modes because they have enough coupling on all five modes. This observation is intuitive when we take a look at the strain energy density map (Figure 2.6): together the three patches cover all the modes maximums, and therefore they have a good damping authority on all of them.

This mean shunt solution with three patches is tested on our model of bladed rail, and compared with an optimised RL shunt.

3.3 Method

The piezoelectric patch was modelled with 3D-elements in Abaqus, as a rectangular box with a thickness of 0.2 mm. By defining different sections, the generated mesh possesses groups of elements, one for the the bladed rail and the others for the patches.

The Abaqus model is imported in the Structural Dynamics Toolbox (SDTools) where the material properties, which include the piezoelectric behaviour, are assigned. SDT is a toolbox on Matlab that allows to run modal analysis on a reduced model and to extract a MIMO (multi-input multi-outpet) State Space model from the finite element model. We consider the primary damping to be low ($\xi = 10^{-5}$). The ceramic used for the piezoelectric transducers is PIC255 (see Table 3.1).

Material property	Value	Unit
d_{31}	-180	$10^{-12}m/V$
d_{33}	400	$10^{-12}m/V$
d_{15}	550	$10^{-12}m/V$
S_{11}	16.1	$10^{-12}m^2/N$
S_{33}	20.7	$10^{-12}m^2/N$
S_{12}	-5.22	$10^{-12}m^2/N$
S_{13}	6.27	$10^{-12}m^2/N$
S_{44}	47.5	$10^{-12}m^2/N$
e_{11}^{σ}	14609.1	$10^{-12}F/m$
e_{33}^{σ}	15494.5	$10^{-12}F/m$
ρ (density)	7800	kg/m^3

Table 3.1 – PIC255 material properties [5]. Physical meaning of the parameters explained in Section 1.2.1.

Five patches are positioned on the bottom surface of the bladed rail under each blade (Figure 3.3 (b)). Each patch has two electrodes, one on the top face - at voltage V - and one on the bottom face - at voltage set to 0. In SDT, the patches are defined as both voltage actuator and charge sensor, which allows us to compute Q/V and to model the shunt as in Figure 3.2 (c) and (d).

In order to assess the efficiency of the damping, the performance index is defined as the displacement of the tips of the blades when forces are applied on those tips, $X_i/F_i, i = 1, ..., 5$. Therefore force actuators and displacement sensors measuring motion along the y-axis (along the length of the rail) are placed on the tips of the blades (see Figure 3.3 (a)).

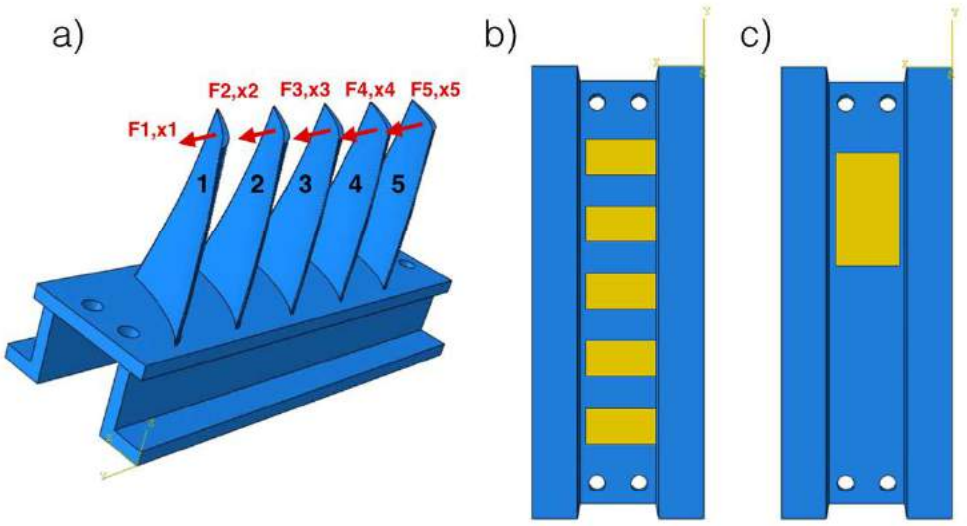

Figure 3.3 – (a) Displacement sensors X_i and force actuators F_i in y-direction are placed on the tips of the blades. The transfer functions X_i/F_i are employed as performance index to assess the efficiency of a damping technique. (b) Patch placement, five patches configuration. The dimensions of each patch are 8.5x16x0.2. In the mean shunt approach, only are shunted the patches under blades 1, 3 and 5. In the H_∞ optimisation, all five patches are shunted. (c) Patch placement, one patch configuration. The dimensions of the patch are 30x17x0.2.

The system extracted from SDT has 10 inputs, 10 outputs. To model the shunts, loops are closed between the voltage inputs - charge outputs, obtaining the overall system illustrated in Figure 3.4. For simplicity purposes, all the loops are constituted of the identical elements. Having to optimise all the components individually would require an optimisation in a 10 dimensional space.

Three types of shunts are evaluated on this system: (1) H_∞ optimal R-shunt, (2) mean RL-shunt, (3) H_∞ optimal RL-shunt. The parameters of the mean shunt are selected adopting the same algorithm employed in [2], and only using three loops (three patches) instead of five. The optimal values of the components for R-shunt and RL-shunt are computed with an H_∞ optimisation with five loops. Concretely, the values are selected in order to minimise the maximum (H_∞ norm) of the transfer functions $X_i/F_i, i = 1, ..., 5$. Other optimisations are sometimes employed: maximisation of damping, H_2 optimisation. In this case, the objective is to decrease the amplitude of the resonances of the structure,

favouring the H_∞ method. The other optimisation methods are thus not considered.

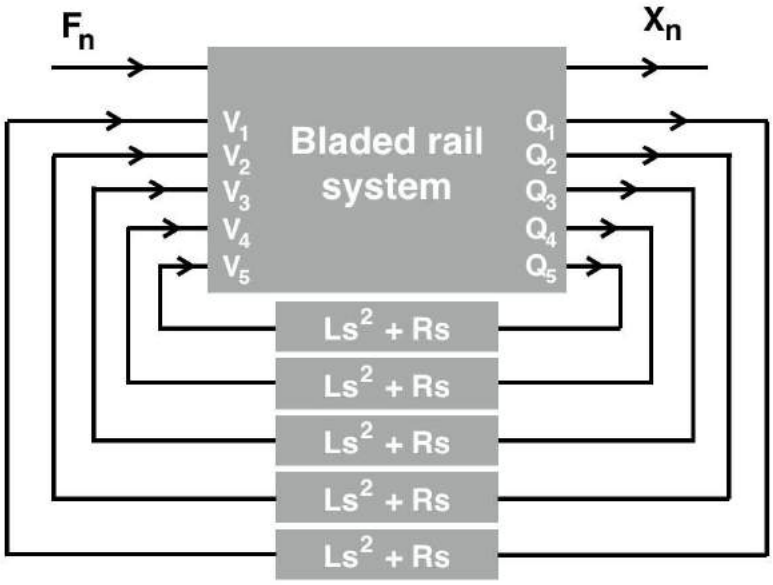

Figure 3.4 – Connection of shunt circuits to the bladed rail MIMO system (10 inputs, 10 outputs). For the R-shunt, the inductance values are set to zero. For the mean shunt approach, the loops between Q_2 - V_2 and Q_4 - V_4 are left open.

The sensibility to circuit mistuning of the mean RL-shunt is analysed calculating how the peak reduction Δp of the transfer functions X_i/F_i diminish when the electrical natural frequency recedes from the mechanical one. The peak reduction Δp is obtained with the following algorithm (ω is the frequency):

$$y_i^0 = \max_\omega \left| \left(\frac{X_i}{F_i} \right)_{undamped} \right|; i = 1, .., 5 \tag{3.16}$$

$$y_j^d = \max_\omega \left| \left(\frac{X_j}{F_j} \right)_{shunted} \right|; j = 1, ..., 5 \tag{3.17}$$

$$\Delta p = \max_{k=1,...,5} 20 \log \left(\frac{y_k^d}{y_k^0} \right) \tag{3.18}$$

Finally the patch placement effect is qualitatively investigated, by implementing the mean shunt on a one-patch configuration system, in which the patch is larger and located on only one side of the rail (see Figure 3.3 (c)).

3.4 Results and discussion

The transfer function Q/V (patch 1) is computed and shown on Figure 3.5. As expected, we observe alternating poles and zeros at the five natural frequencies of the first family of modes. From the Q_i/V_i transfer functions, we can deduce: K_{ij}, the effective electromechanical coupling factors (for patch i and mode j) using the equation 3.6, enabling the evaluation of the mean shunt resistance value (Eq. 3.13); C_{stat}, the static capacitance, obtained when the frequency is equal to zero; and the average frequency $\overline{\omega}$ from which the

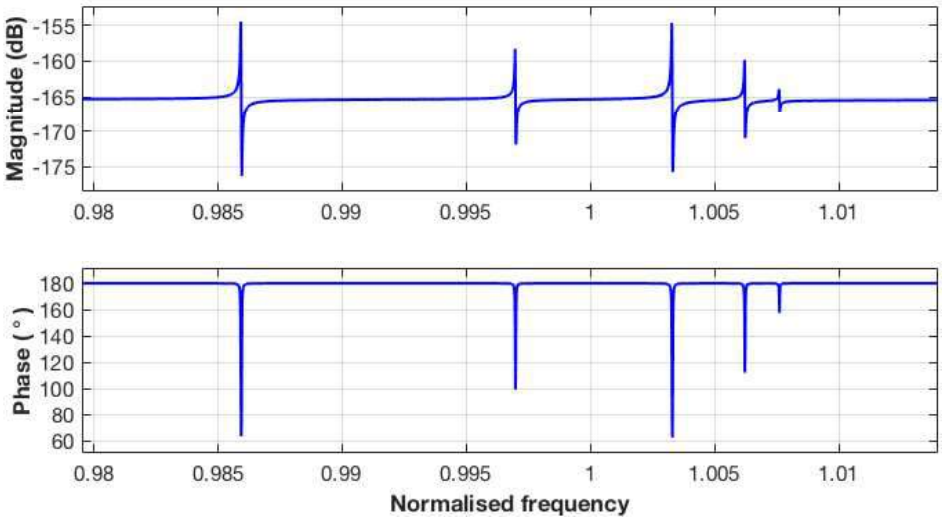

Figure 3.5 – Bode diagram of Q_1/V_1 (patch 1) zoomed on the first family of modes. The frequencies are normalised dividing them by the mean frequency of the first family of modes. As expected, there are alternating poles and zeros at the natural frequencies.

inductance is calculated (Eq. 3.12). Those parameter values are displayed in Table 3.2, compared with the H_∞ optimal values.

Shunt type	C_{stat}	R	L
R shunt	5.3785 nF	24437.4 Ω	0 H
Mean shunt	5.3785 nF	1193.0 Ω	3.0466 H
H_∞ RL shunt	5.3785 nF	649.5 Ω	3.0355 H

Table 3.2 – Electrical components values for each type of shunt

It can be noted that the value of the inductance is almost identical for the two RL shunts, which is logical as the electrical natural frequency needs to equalise the mechanical one to be optimal. The value of the resistance however changes. It is because the mean shunt approach originated from the approximation of an optimisation. Therefore the value of the resistance obtained differs. The effect of the shunt strategies can be seen on Figure 3.6.

Not surprisingly, the R-shunt is the least effective. However it is a broadband strategy and thus it could be an interesting option to exploit if the other families of mode were to be damped as well. As it is not tuned on a particular frequency, it is not affected by any circuit mistuning or lack of knowledge on the structure natural frequencies.

The best RL-shunt is naturally the one obtained by H_∞ optimisation, at least when the performance is assessed by the amplitude of the transfer functions, as the optimisation aims to minimise it.

Even so, the mean shunt approach exhibits many advantages: it only requires three patches over the five, which also implies less electronic components, and it does not need a complete simulation to select the parameters. When the optimisation demands a full simulation model, the mean shunt components values can be deduced directly from experimental data, as long as the transfer functions Q_i/V_i are measured.

The resonant shunts sensibility to circuit mistuning is checked by calculating the peak

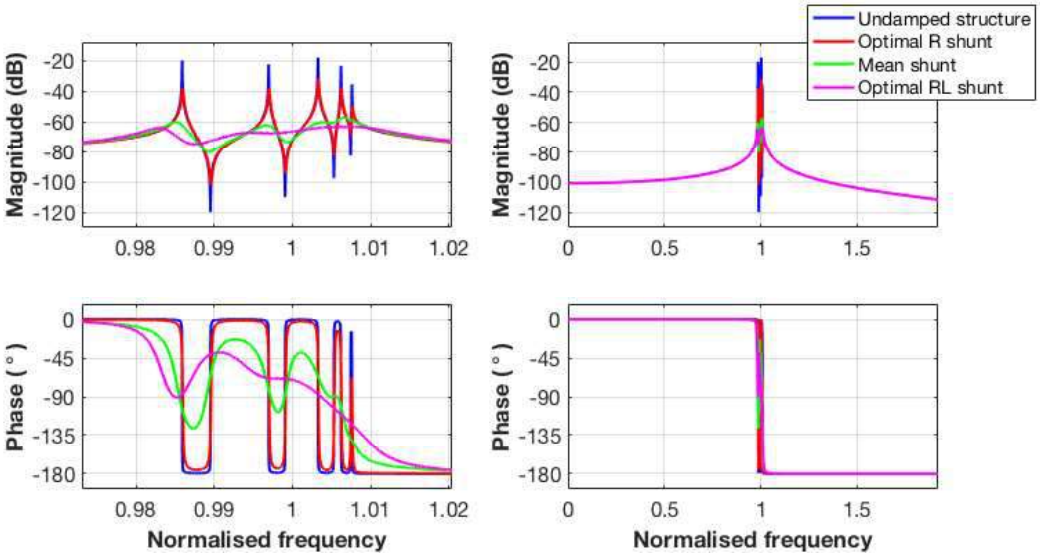

Figure 3.6 – Effect of the damping techniques on the bode diagram of X_1/F_1, zoomed on the first family of modes. Panel left is a zoom on the peak of panel right. We clearly see that RL shunts are more efficient than their purely R shunt counterpart.

attenuation with the algorithm described by Eq. 3.16, 3.17, 3.18. The result is plotted on Figure 3.7.

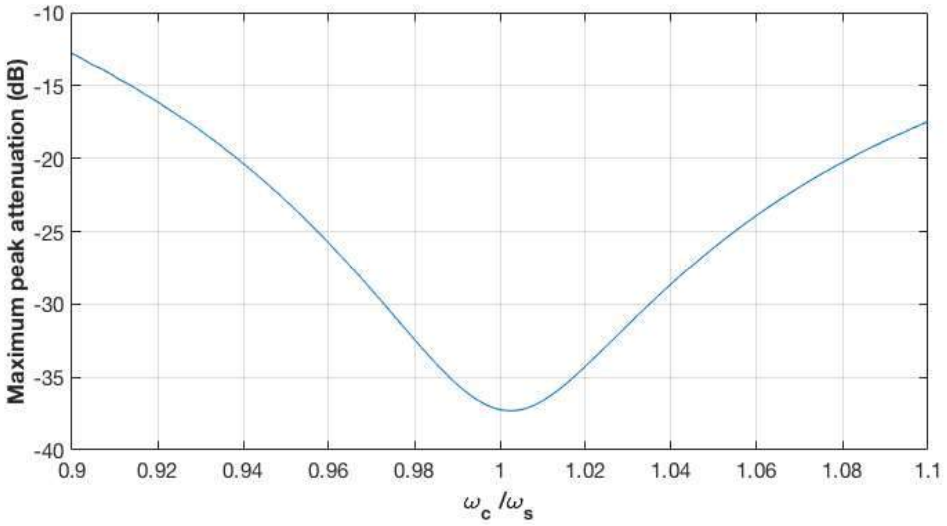

Figure 3.7 – Maximum peak attenuation when shunt circuit electrical frequency is mistuned. An error of 10% can result in a loss of vibration reduction of more than 20 dB.

It is clear, from this graph, that mistuning is a real issue for RL shunts, as its efficiency drastically decreases if the components in the electrical circuit are not determined accurately. An deviation of 10% from the optimal electrical frequency can result in a loss of resonance peak reduction of more than 20 dB.

The patch placement effect results are shown in Figure 3.8. In both configurations illusatrated in Figures 3.3 (b) and (c), the RL shunts components are determined by the mean shunt approach. From the results, it appears that the patch placement or size influ-

ence is quite significant, as they are some noticeable consequences: the higher frequency modes are less damped for the one-patch configuration because we see on Figure 2.5 that it covers opposite sign displacements for modes 3 to 5. It means that for those modes, the patch is bending in two opposite ways, which cancels the piezoelectric coupling as the accumulated charges add up to zero. It explains why higher modes are less damped. The best way to equally damp the five modes is to ensure no patch is located on two opposite maximums, which is achieved by placing one patch under each one of them, that is under each blade.

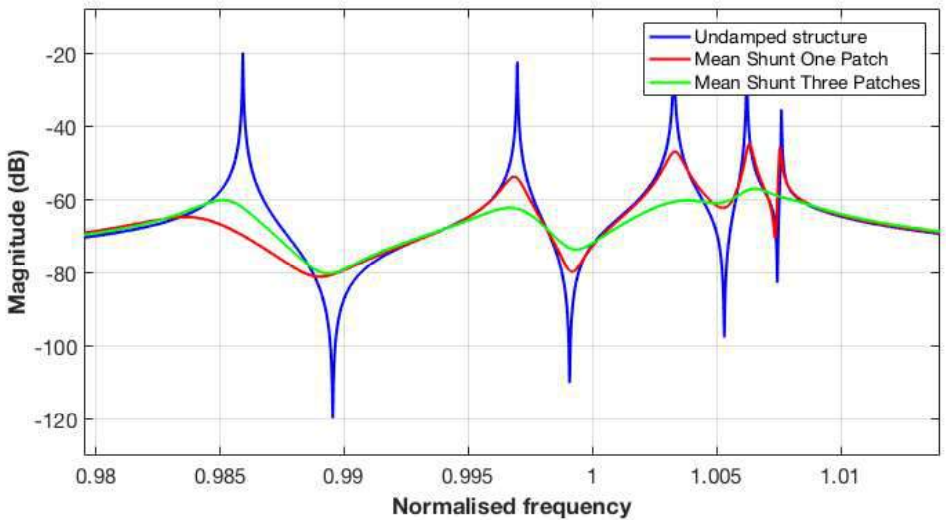

Figure 3.8 – Effect of the patch placement on the bode diagram of X_1/F_1, zoomed on the first family of modes, comparing the configuration with five patches with one with only one bigger patch (Fig. 3.3 (c) and (d). The bigger patch damps effectively the first modes, but loses performance on the higher frequency modes.

3.5 Conclusion

The broadband and the resonant piezoelectric shunts have been introduced and applied to the bladed rail model. Five piezoelectric patches, in the form of a rectangular box, have been added to the bottom surface of the bladed rail, under each blade. A State Space model was then extracted from SDT (Structural Dynamics Toolbox).

Two kinds of shunt circuits have been exploited, connecting independent identical circuits to each patch. To optimally tune the parameters of the shunts, H_∞ optimisation has been proposed. Its efficiency has been compared to the shunted system when the parameters are selected according to mean approach.

As expected, resonant shunts are more effective than purely R-shunts to damp closely located modes. However, RL shunts exhibit a strong dependence on the electrical frequency tuning, and therefore a special care should be given to accurately know the resonance frequencies of the structure and the value of the electrical components employed.

Selecting the RL-shunt parameters by H_∞ optimisation exposes slightly better results in terms of peak attenuation than the mean shunt approach. However the mean shunt approach is very useful if no simulation model is available and that parameter selection must be done with only experimental data.

The passive damping techniques developed in this chapters show positive outcomes. The next part of this study seeks to improve them by introducing active damping.

Chapter 4
Active damping

Chapter summary Piezoelectric active damping relies on the use of control sources to inject a signal into the mechanical system through piezoelectric transducer actuators. The signal is determined by a control law and piezoelectric sensor information in order to damp the unwanted vibrations created by excitation sources. Collocated actuators and sensors allow to apply some well-known stability guaranteed control strategies. Five pairs of piezoelectric patches actuators and sensors are added to the bladed rail 3D-model. The retained size of the patches depends on their collocated nature and their damping potential. Integral control and Resonant control (Negative Position Feedback) are applied to the system and compared in terms of performance and stability robustness. Finally, recommendations based on the results of active and passive damping are made.

4.1 Introduction

The idea of employing active sound cancellation to replace passive control was first introduced by Coanda in patents published in the early 1930s [28]. After that (1936 and 1937), Paul Lueg published patents containing more accurate physical explanations, illustrating the principles of the method on the case of acoustic waves cancellation propagating in a duct. His work is from then often cited as the beginning of active noise and vibration control.

Active vibration control systems use one or more control sources to inject a controlling disturbance into the structural system, aiming to reduce the unwanted vibrations generated by excitation sources. The signals that drive the control actuators are produced by an electronic controller, which takes as inputs, measurements of the state of the system provided by sensors after the injection of the control signal.

Piezoelectric transducers exhibit excellent actuation and sensing abilities which originate from their good electro-mechanical coupling coefficient. Adding to that fact their non-intrusive nature and their application flexibility, piezoelectric materials form very suitable candidates for active vibration control, exploited as sensors, actuators or both. P. Shivashankar and S. Gopalakrishnan (2020) [18] propose a review of the technology, listing many applications, control laws and optimisation algorithms from the literature .

The actuator and sensor placement is an essential step in active damping designs. When they are attached to the same degree of freedom, they are said collocated and allow to implement control techniques with robust stability [26].

Two active damping strategies are applied on the bladed rail, using numerical optimisations to tune their parameters, in the same way it was achieved with the piezoelectric shunts. The first one is a broadband controller, employing an integrator: the Integral Feedback. The second one is a resonant controller, the Negative Position Feedback, targeting specifically the first family of modes. The choice of those dampers is justified in following sections.

This chapter addresses the active damping design process. At first, some theory concepts about collocated systems are established in order to decide the most adequate actu-

ator and sensor placement on the bottom of the bladed rail. Subsequently the two control strategies are explained. These are simulated and the results are presented in a last section, compared with the passive damping techniques results.

4.2 Active damper design

Active damping is a class of active control that requires little control effort, called Low Authority Control. Its objective is to increase the negative real part of the system poles, which differs from other techniques that completely relocate the closed-loop poles (natural frequency and damping).

Active damping is recommended if higher control authority is required on several modes, or when it is easier to implement than passive techniques, for example when the structure already includes actuators and sensors. Nevertheless the method demands an external power source. This can be an issue for some applications in which the power consumption is a key factor.

In this project, the conception of active damping systems is organised in three phases: (1) actuator and sensor determination and placement, (2) closed-loop design, (3) stability analysis. Naturally the three steps are very connected, and a choice made at one of them impacts the rest.

4.2.1 Actuator and sensor pair

The positioning of the actuators and sensors is crucial to build high performance damping systems. There are two main concerns about the issue that are associated to mode authority and to control stability.

The controller authority on a mode strongly depends on independently the position of the actuators and the sensors. If the actuator is placed on mode shape nodes, it will never be able to excite that mode, and therefore there will be no possibility to damp it. Similarly, if the sensor is on a node, it will not detect vibrations, which impedes a feedback control. Hence the actuators and sensors should be placed on mode shapes maximums.

Actuator and sensor placement also needs to fulfil control stability requirements. If, for example, they are attached on structure at two very different locations, what is measured by the sensor is used by the actuator located where that information is possibly irrelevant. Those configurations generate sensitivity loss and delays in the controller, and make the design of stable damping systems more complicated.

The motion of a dynamical structure $y(x,t)$ is described in the modal space as a linear combination of generalised displacements (degrees of freedom) $z_i(t)$ and mode shape $\phi_i(x)$ (N is the number of modes, x the position and t the time):

$$\sum_{i=1}^{N} \phi_i(x) z_i(t) \tag{4.1}$$

The transfer function between the actuator input u, placed in x_a, and the sensor output v, in x_s, for a lightly damped structure, is [29]:

$$\frac{v(x_s)}{u(x_a)} = \sum_{i=1}^{N} \frac{\phi_i(x_s)\phi_i(x_a)/\mu_i}{s^2 + 2\xi_i\omega_i s + \omega_i^2} \tag{4.2}$$

where ω_i is the natural frequency of the structure for mode i, ξ_i the corresponding modal damping, and μ_i the modal mass.

If the actuator and the sensor are located on the same degree of freedom ($x_a = x_s$), they are said collocated. The Equation 4.2 becomes:

$$\frac{v(x_a)}{u(x_a)} = \sum_{i=1}^{N} \frac{\phi_i^2(x_a)/\mu_i}{s^2 + 2\xi_i\omega_i s + \omega_i^2} \tag{4.3}$$

where the numerator is consequently always positive. A typical characteristic of collocated systems transfer functions is the presence of alternating poles and zeros, moved a little in the left-half plane (see Figure 4.1). This property guarantees good stability properties for a wide class of control systems.

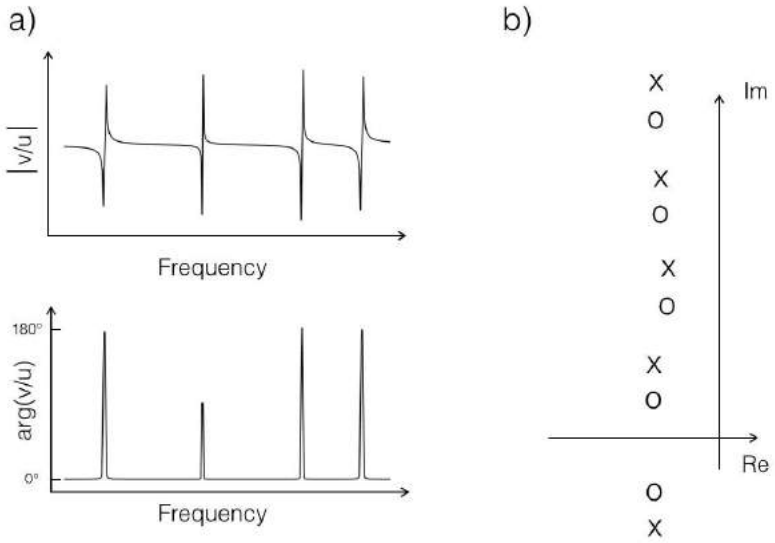

Figure 4.1 – (a) Bode diagram of a system with collocated actuator (input signal u) and sensor (output signal v). The transfer function presents an alternating zero-pole pattern. (b) Plot of the $\frac{v}{u}$ transfer function poles (designated by X) and zeros (designated by O) in the complex plane. As the system is lightly damped, the poles and zeros are all found slightly to the left side of the plane.

When the transfer function has interlacing poles and zeros even when the actuator and sensor are not on the same degree freedom, the actuator/sensor pair is nearly collocated. It means that the numerator of Eq. 4.2 is positive for all modes i, which means:

$$sign(\phi_i(x_s)) = sign(\phi_i(x_a)) \tag{4.4}$$

In the case of the bladed rail, the actuators and sensors are piezoelectric transducers (patches) bonded to the bottom surface. Their input and output signals are voltage related to the strain in the patches by Eq. 1.1 and 1.2, electrically corresponding to the circuit in Figure 4.2.

The patches are clearly not linked to the same degree freedom, as they are covering different areas on the bladed rail. The objective is to find locations in which the pairs of actuator and sensor patches are nearly collocated. This is achieved making sure the sensor and actuator of a same pair are measuring the same sign of the mode shape, for

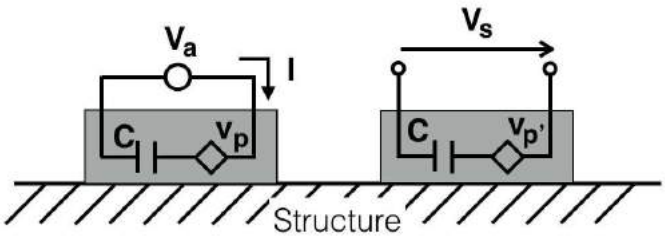

Figure 4.2 – Electrical representation of piezoelectric patches mounted on a structure surface. The left patch is used as an actuator where a voltage V_a is injected. The right patch plays as sensor where a voltage V_s is measured at its electrodes.

all the modes. We will observe in the results of the simulations that it is possible to reach such control systems, exhibiting an interlacing zero-pole pattern (with zero before pole as is Figure 4.1). Once the right configuration of patches is found, a control can be implemented.

4.2.2 Control strategies

Designing a control strategy relies in connecting a feedback loop from the sensor to the actuator, defining the kind of controller $H(s)$ and the related gain g used in the loop (illustrated in Figure 4.3). Collocated actuator and sensor allow the implementation of collocated control techniques that exhibit stability even at high amplitude of the gain.

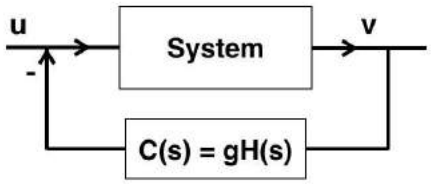

Figure 4.3 – Negative feedback loop with a controller C(s).

As for their passive counterparts, the active damping techniques are either broadband (first order method), equally damping all the modes, or resonant (second order method), targeting specific modes. In this case, an integral control and a second order negative position feedback are designed and implemented.

Integral control The transfer function between the piezoelectric sensor and actuator patches shows an alternating zero-pole pattern, with zero before pole. According to Preumont (2011), an appropriate broadband damping technique to be used is an integral control (Integral Force Feedback [26]):

$$C(s) = \frac{g}{s} \tag{4.5}$$

For a single-input single-output collocated system, the method is unconditionally robust, as, for any gain, the poles of the closed loop are always located in the left side of the complex plane (negative real part). Applied to the bladed rail, its robustness is not unconditional,

but is still very good. Besides the controller is easy to optimise as it only depends on one parameter.

Negative Position Feedback As for the resonant passive absorbers, resonant controllers are excellent candidates to affect particular modes. The Positive Position Feedback is often proposed for that purpose when dealing with collocated systems [26][3]. The method is considered robust, because it only becomes unstable for extensively high gains. However the technique is only fitted for a pole before zero pattern in the sensor/actuator transfer function. In order to adapt the method to this case (zero before pole pattern), the sign of the loop can be changed, giving a Negative Position Feedback. The controller becomes:

$$C(s) = \frac{g}{s^2 + 2\xi_f \omega_f s + \omega_f^2} \tag{4.6}$$

where $g > 0$, $\omega_f > 0$, $0 < \xi_f < 1$ are parameters to tune depending on the targeted modes.

MIMO multi-mode adaptation In this project, five pairs of collocated actuator/sensor patches are attached on the bottom surface of the bladed rail. The system therefore becomes multi-input multi-output (MIMO). This allows to conceive one feedback loop for each pair. However the implementation of a feedback loop on one pair affects the transfer function of the other pairs. This interdependence has to be acknowledged and the optimum design of the controllers has to be executed simultaneously, assessing the efficiency of the five feedback loops combined.

The bladed rail is also a multi-mode structure. In this project, as mentioned before, the objective is to damp the first family of modes. The controllers parameters will be selected for specifically those targeted modes. In order to simplify the design, the five feedback loops are chosen identical, dividing the number of parameters by five.

4.2.3 Stability and robustness

A control system is robust if its stability is not affected by controller parameters perturbation. The robustness of an active control system must always be assessed. In general, more robustness means less damping performance, and vice versa, which leads to a classical design trade-off.

For single-input single-output (SISO) systems, the gain and phase margins (i.e. the gain and phase allowed deviation of the controller before it becomes unstable) is directly deduced from the Bode diagram of open-loop transfer function (see [30] for more information about the procedure). In the case of MIMO systems, this method no longer applies.

This control design is constituted of five identical feedback loops, tuned with the same parameters. Alternative gain and phase margin can be computed by plotting the poles location on the complex plane when the gain or the phase of the controller is equally modified in each loop, giving respectively a new gain margin or phase margin (see Figure 4.4).

Stability robustness can be affected by modes at much higher frequencies than the ones we are interested in, as the collocated characteristic of the system can be lost. Yet real continuous structures have infinite resonances, and of course, numerical models can not include all of them, discarding then higher modes (truncated model). This lack of information at higher frequency must be kept in mind, as those modes could invalidate a stability deduced numerically from a truncated model.

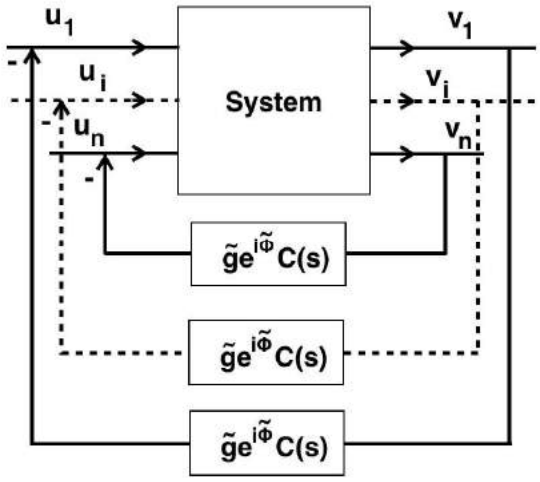

Figure 4.4 – MIMO control robustness evaluation. For a system where the feedback loops are identical, the gain and the phase of the controller $C(s)$ can be changed simultaneously in all the loops (multiplying it by $\tilde{g}e^{i\tilde{\Phi}}$). The value of $\tilde{g}$ (resp. $\tilde{\Phi}$) from which the closed loop system becomes unstable is considered as the gain margin (resp. phase margin).

4.3 Method

This time, ten piezoelectric patches were modelled with 3D-elements in Abaqus on the bottom surface of the bladed rail. Three configurations are treated involving different patches sizes, see Fig. 4.5. By defining different sections, the generated mesh possesses groups of elements, one for the the bladed rail and the others for the patches. With SDTools, a MIMO State Space model extracted from the Abaqus model, reduced at the twenty first modes. Again, we consider the primary damping to be low ($\xi = 10^{-5}$) and that the piezoelectric transducers are formed of PIC255.

The piezoelectric patches are organised in pairs, each containing side by side an actuator patch and a sensor patch. We write V_{ai} the voltage input applied to the actuator patch of pair number i and V_{sj} the voltage output measured at sensor patch of pair number j. Those pairs are shown on Figure 4.5. For each configuration, for each pair, the actuator patch and sensor patch are placed close to each other with the intention to create (nearly) collocated actuator and sensor pairs. Different configurations are tested in order to find that ideal case. To that end, the transfer functions V_{si}/V_{ai} $(i = 1, ..., 5)$ are computed and inspected for each configuration to determine if they present an alternating pole-zero pattern, characteristic of collocated systems.

Once the collocated behaviour of a configuration is verified, a control feedback loop is connected between the sensor and actuator of each pair, see Fig. 4.6. In the same way as for the passive damping (see Chapter 3), the efficiency of the designed control technique is assessed with the amplitude of the transfer functions between the forces applied on the tips of the blades and their consecutive displacement X_i/F_i (for blade i), see Fig. 3.3.

The bladed rail MIMO system extracted from SDT has 10 inputs, 10 outputs, and five feedback loops. For application simplicity purposes, all the loops are constituted of an identical controller $C(s)$.

Three controllers are evaluated: one integral controller and two negative position feedback controllers containing distinct parameters (resonant controller I and II). To optimise

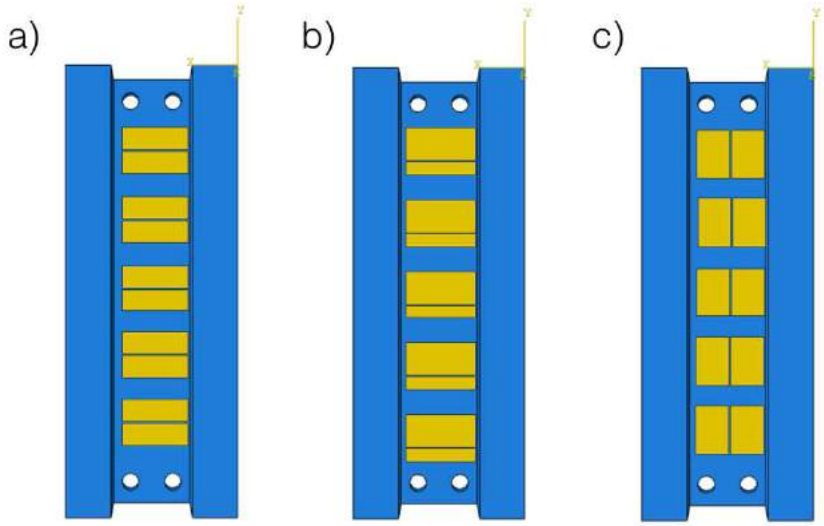

Figure 4.5 – Active damping configurations with five pairs of piezoelectric actuator and sensor patches located under the blades. (a) The actuator (on the top) and the sensor (bottom) of a pair have the same dimension: 15x5x0.2. (b) The actuator (on the top) and the sensor (bottom) of a pair have different dimensions: 16x7.5x0.5 (actuator) and 16x3x0.5 (sensor). (c) The actuator (on the right) and the sensor (on the left) of a pair have the same dimension: 11x7.5x0.5.

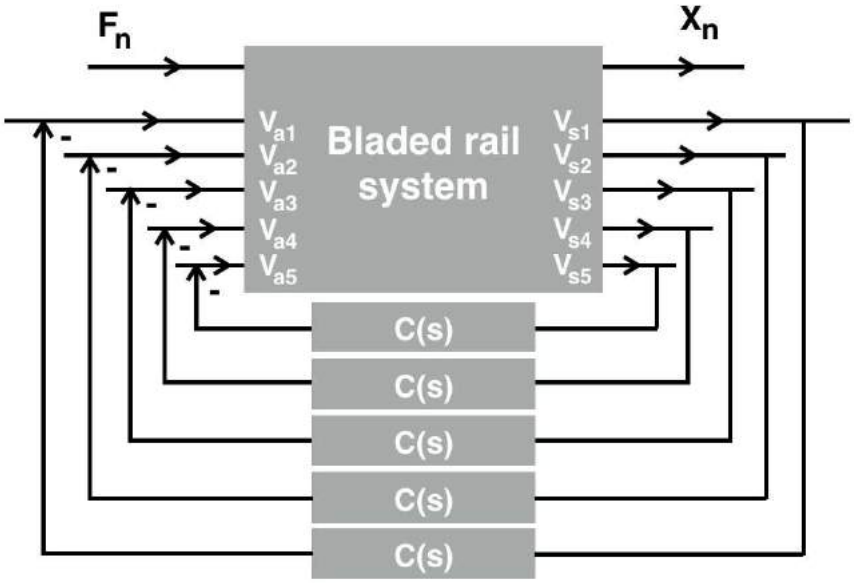

Figure 4.6 – The bladed rail system is controlled by five identical feedback loops that connect the sensor to the actuator of each pair of patches. The performance of the control strategy is assessed by the transfer functions X_n/F_n.

the parameters, two kinds of optimisation algorithms were used, and only the best result was retained. The first one consists in the H_∞ optimisation previously introduced (see Chapter 3). The second one is based on maximising the minimum modal damping for the first family of modes (damping maximisation).

The gain and phase margins are obtained according to the MIMO Robustness procedure

described by Figure 4.4. The resonant control I parameters are computed by restraining the space of the optimisation problem solutions to controllers with sufficient gain $G_m > 10dB$ and phase margin $P_m > 15°$.

Finally, the active damping methods are compared to the best result obtained with passive damping: the optimal RL shunt.

4.4 Results and discussions

The transfer functions V_{si}/V_{ai} (for each pair i) were computed and are presented in Figures 4.7, 4.8 and 4.9. On Figure 4.7 are displayed the transfer functions V_{s2}/V_{a2} of the configurations (a) and (c) (see Fig. 4.5) zoomed on the first family of modes. Configurations (a) and (b) (not displayed here) are exhibiting a collocated behaviour for all five pairs at low frequency (first family of modes frequency range), with a zero-pole pattern. Configuration (c), however, does not have collocated sensor and actuator pairs, as observed in Figure 4.7.

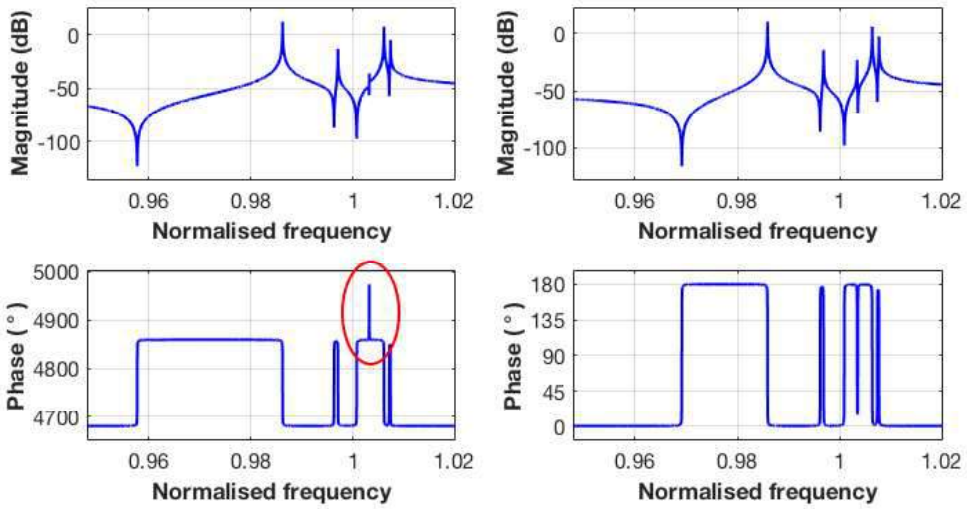

Figure 4.7 – Transfer functions V_{s2}/V_{a2} zoomed on the first family of modes for the configurations (a) (on the right) and (c) (on the left) (see Fig. 4.5). While configuration (a) has interlacing zeros and poles, configuration (c) shows a discontinuity of that pattern for mode 3, where the pole comes before the zero (as highlighted by the change of phase in the red ellipse). It is a non-collocated behaviour.

On Figure 4.8, the transfer function V_{s5}/V_{a5} of configuration (a) is plotted for a wider range of frequency. We see that at approximately twice the first family of modes average frequency the zero pole pattern is broken. It illustrates that a collocated system at low frequency is probably loosing its collocated behaviour at higher frequency. And as the models used are truncated (at the 20th mode), it is fair to assume that the pattern will be lost at high frequency even if it is not visible in our models. For the purpose of this project, the configurations are considered valid if the system is collocated at the first family frequencies: configurations (a) and (b).

Difficulties were encountered during the simulation regarding the position of the first zero appearing in the V_{si}/V_{ai} transfer functions. This positions varies strongly with the number of finite elements that constitute the piezoelectric patches in the 3D-model. This

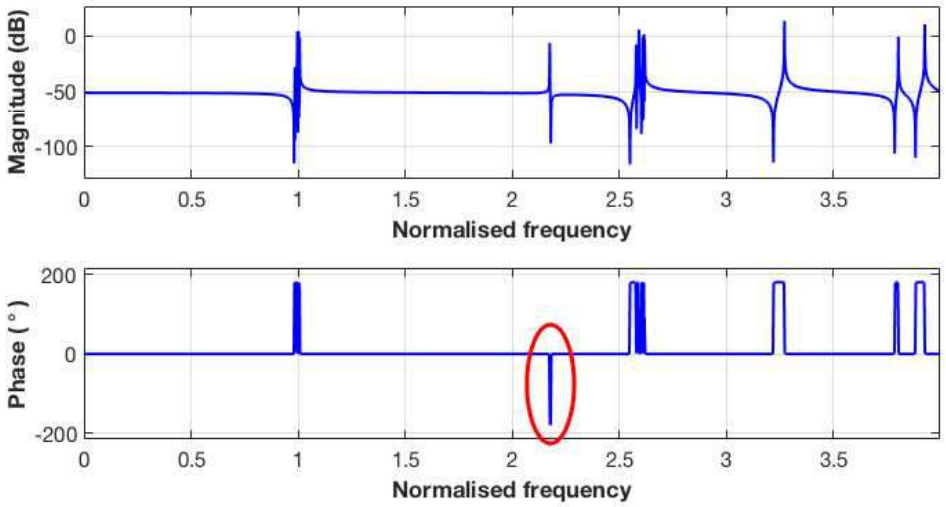

Figure 4.8 – Transfer function V_{s5}/V_{a5} of configuration (a). The sixth mode breaks to zero-pole pattern by exhibiting a pole before zero. It shows that the system looses its (nearly) collocated behaviour at high frequency.

phenomenon is exposed on Figure 4.9 for the transfer function V_{s3}/V_{a3} of configuration (b). When the mesh becomes finer on the patch, the zero shifts to lower frequencies. This revealed that the model was not converged for the position of the first zero. We tried to reach the convergence by reducing even more the size of the elements composing the patches but the model became too heavy to process. This still unsolved issue highlighted the need to obtain experimental curves for the transfer functions.

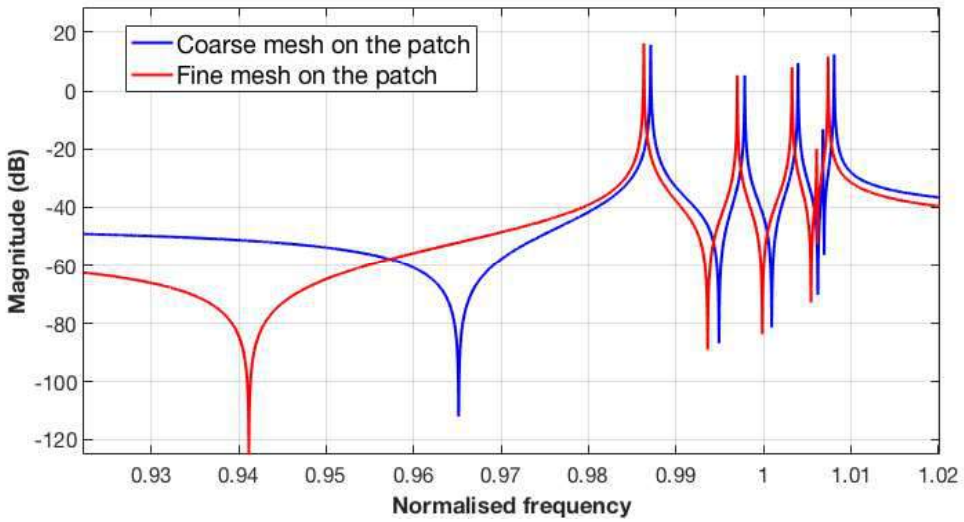

Figure 4.9 – Transfer function V_{s3}/V_{a3} of configuration (b) zoomed on the first family of modes. The blue curve corresponds to the simulation model with a coarse mesh on the patches (element size 2 mm). The red curve corresponds to a fine mesh on the patches (element size 0.5 mm). Adding elements makes the structure softer, which explains the slight translation of the natural frequency peaks. The first zero position varies a lot with the mesh on the patch.

The model with a coarse mesh on the patch was preserved for the control design, acknowledging that the first zero position is uncertain and that it could affect the design validity.

Optimisations were run for configurations (a) and (b). The damping efficiency reached in configuration (a) appeared to be better than the one reached by (b) (shown in Appendix B). Moreover, configuration (a) involves patches of the same size for the sensors and actuators, which eases its practical implementation. Those facts lead us to focus on configuration (a). The results are presented in the following paragraphs.

The three controllers parameters were selected by the maximum damping optimisation (H_∞ did not provide as good optimums). Controllers robustness was assessed, computing the MIMO gain and phase margins. This data is reported in Table 4.1.

Controller type	g	ω_f	ξ_f	G_m (dB)	P_m (deg)
Integral control	$2.5337\ 10^6$	-	-	18	78.5
Resonant control I	$8.7580\ 10^7$	7876.5	0.0163	33.9	15.9
Resonant control II	$1.0645\ 10^{10}$	5868.4	0.1701	10.1	4.2

Table 4.1 – Parameter values for each type of controller and corresponding gain and phase margins

The performance of the controllers is evaluated by the peak reduction observed in the transfer functions X_i/F_i (for blade i). On Figure 4.10, one can see the damping effect of the controllers for blade 1.

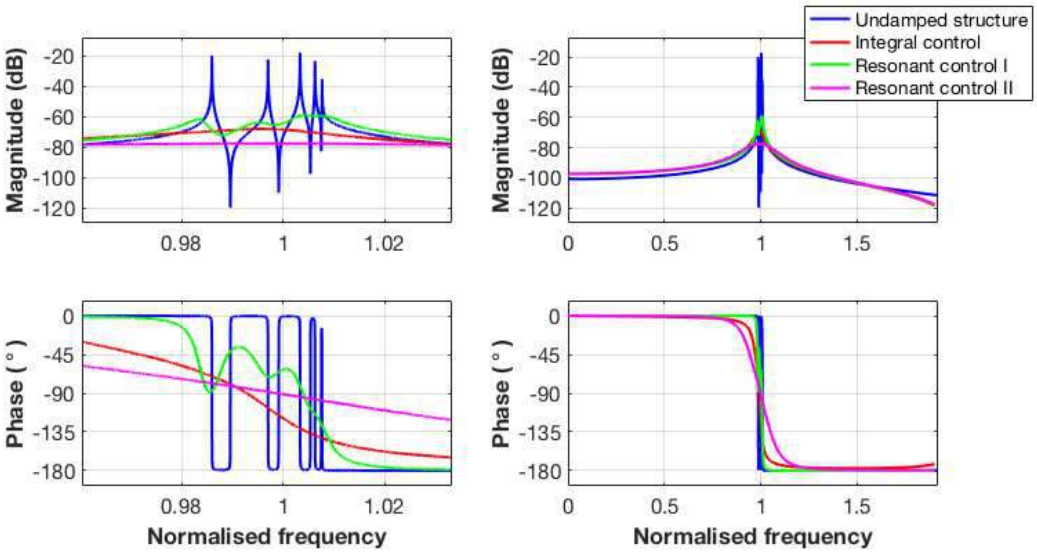

Figure 4.10 – Effect of the active damping techniques on the bode diagram of X_1/F_1, zoomed on the first family of modes. Resonant control II provides the strongest peak reduction.

According to these results, the performance of the resonant control II is excellent, allowing a peak reduction of 15 dB more than with integral control. This ideal controller is however very complicated to implement in practice because of its lack of robustness. Whereas its gain margin is acceptable, a phase margin of 4.2° is way too small.

Resonant control I was obtained by imposing minimal gain and phase margins. Augmenting the phase margin to 15.9° reduces significantly the damping performance of the

controller (of more than 10 dB).

The integral control exhibits similar performance to the resonant control I. Nevertheless it possesses a much higher phase margin (78.5°) and a good gain margin, which makes it more interesting in terms of robustness. In addition, because it is broadband, the integral control is able to damp all the modes, not only the ones of the first family.

From those results, we can say that, if a very low phase margin can be handled, the resonant control II is the most suited to damp the first family of modes. But if this is impossible in practice, the integral control offers the best compromise between performance and robustness.

The active damping performance results are compared to the optimal RL shunt damping obtained in Chapter 3, see Fig. 4.11.

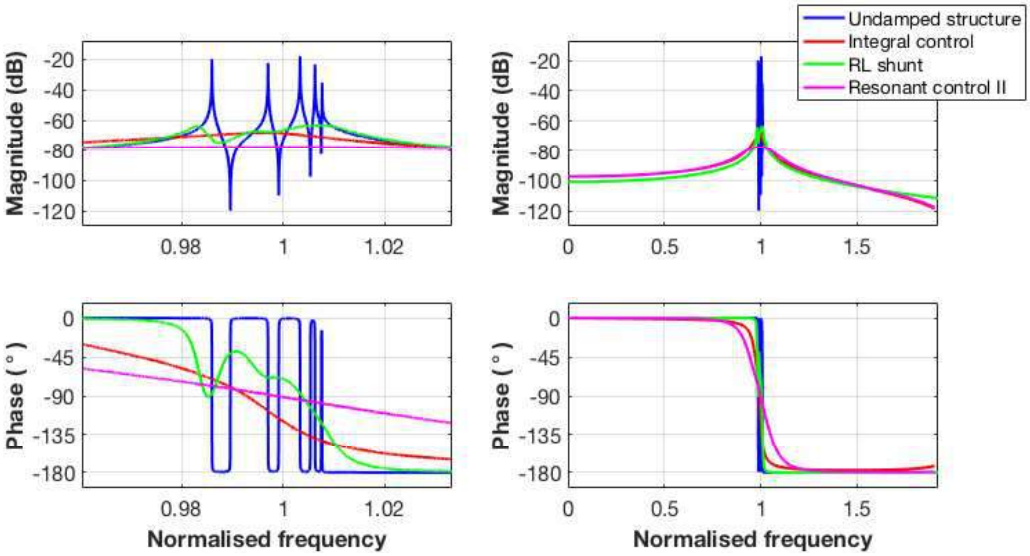

Figure 4.11 – Effect of the active damping techniques on the bode diagram of X_1/F_1, zoomed on the first family of modes, in comparison with the optimal RL shunt technique.

Comparing the different techniques, it appears that the integral control exhibits slightly better results than the RL shunt technique, reaching until 10 dB of improvement for the fifth mode damping. Still the result of those two methods is quite similar for the first family of modes. The choice between them depends on what advantage of each is most valuable: on one hand, the RL shunt does not require external power source but only affects the first family of modes and is very sensitive to mistuning; on the other hand, the integral control requires external power source but is broadband and thus not only damps the first family of modes.

4.5 Conclusion

Three configurations with five pairs of actuator and sensor piezoelectric patches were modelled through SDTools and investigated. One of them prevailed as it exhibits a (nearly) collocated behaviour and a good performance. The transfer functions between the actuator patches voltage inputs and the sensor patches voltage outputs seem not to have completely converged, as the position of the first zero shifts when the mesh on the patches is refined.

Active damping techniques were designed and applied to the bladed rail. As a result, we observed that the Negative Position Feedback control (resonant control II) provides

the best damping performance. However, its very low robustness complicates its practical implementation.

The Negative Position Feedback control with improved robustness (resonant control I) and the integral control exhibit inferior performance, but better stability robustness. They both damp similarly the first family of modes. But the integral control proves itself to be more propitious as its robustness is considerably better, and it is broadband, allowing to also damps higher modes.

Finally the active and passive damping techniques were compared. As a result, if performance is preferred at the cost of stability robustness, the Negative Position Feedback control (resonant control II) remains the best option. Otherwise, integral control or RL optimised shunt should be favoured, choosing one of them depending on the most limiting factor between requiring external power source (integral control), but with broadband damping, and only being able to damp the first family of modes, being very sensitive to mistuning, but without needing external power source (RL shunt).

In any case, the conclusions obtained so far are based on simulations. As confirmed by the problem of zero shifting in the transfer functions depending on the mesh, an experimental validation is required, destined to confront the simulation model and the related damping performances.

Chapter 5

Experiments

Chapter summary In order to corroborate the simulation results, experiments are performed on an aluminium 3D-printed bladed rail. Five pairs of piezoelectric actuator and sensor patches are glued on the bottom surface of the support. Experimental issues are treated, concerning the manufacturing limitations, piezoelectric plates constraints and external excitation compromise. The empirical transfer functions between the actuator and sensor patches are obtained, allowing to create a model and to initiate the design of a resonant controller for active damping.

5.1 Introduction

The simulation results are promising and provide a good indication of the kind of damping that can be applied on the bladed rail. However the model needs to be confronted to experimental validations to demonstrate the validity of the techniques we proposed.

To that end, an aluminium 3D-printed prototype was built, based on the 3D-model, see Fig. 5.1. Ten piezoelectric plates were attached on the bottom surface, as it was realised in the simulations.

The objectives of conducting experiments on the bladed rail are to corroborate the model and to assess the damping strategies. For this project, only the first one is addressed, the rest of the experimental labour being left to future studies.

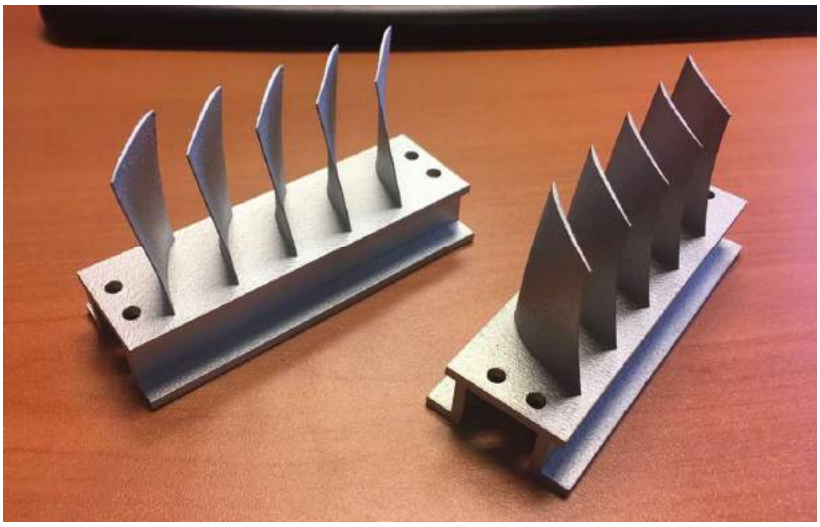

Figure 5.1 – Picture of two 3D-printed bladed rail prototypes.

In this chapter, an analysis of the experimental issues and challenges is proposed. The experimental setup is then explained and the results are presented. To conclude, recommendations for further experiments are made.

5.2 Experimental challenges

There are several differences between the real-life bladed rail and the simulation model, which cause difficulties at the time to reproduce experimentally simulation setups. Those issues involve prototype manufacturing characteristics, piezoelectric transducers application and external excitation.

5.2.1 Manufacturing process

In the industrial sector, blisks are manufactured with very precise machining techniques, such as milling with 5-axis machines [31]. Such method was impossible to implement on the bladed rail at laboratory level for reasons of cost and lack of skilled providers, as the complex shape of the blades hinders the use of conventional machining processes.

In that context, the adoption of additive manufacturing was the cheapest and more reliable alternative. The method employed is called Selective Laser Melting (SLM). It consists in a powder bed fusion process that relies on a high-power density laser as an energy source to melt and merge specific regions of powder, layer by layer [32].

In this case, the prototype was fabricated with an aluminium alloy AlSi10Mg. According to the literature, the relative density of SLM aluminium products can reach 99.50 %. In terms of mechanical properties, the alloy is similar to the aluminium used in traditional manufacturing, see Table 5.1. A strong limitation however relies in the surface quality. The arithmetic average roughness of those products was reported to be approximately equal to 15 μm. On Figure 5.2, one can observe the very rough surface of the bladed rail prototype produced by SLM. This creates a disparity with the simulation model, but also with the real bladed disks, for which the surfaces provided by machining are much smoother.

Figure 5.2 – Picture of the bottom surface of the bladed rail prototype. The high roughness of the surface is visible at naked eye.

Surface roughness is not a problem for vibration analysis. However it possibly changes the interaction between the structure and the mounted piezoelectric patches.

Type	Density (kg/m^3)	Young Modulus (MPa)	Poisson Coefficient
Aluminium	2700	70000	0.30
AlSi10Mg	2650	68000	0.32

Table 5.1 – Aluminium mechanical properties comparison - Classical aluminium alloy [4] and SLM AlSi10Mg [6][7]

5.2.2 Piezoelectric patches

Ideally, the piezoelectric patches should be mounted on the bladed rail with direct bonding between the transducer and the structure surface. This is the case in simulation, where piezoelectric elements are directly linked to the primary structure elements. The mechanical deformation of the structure is thereby transferred to the patches without interface.

In reality, the patches are glued to the host surface. It means there is an interface between the transducer and the structure. This adhesive layer is less stiff, more viscous and can generate some nonlinear effects that modify the interaction between the host surface and the transducer. These effects have been studied and modelled, see [33], [34], [35]. It is possible in practice to avoid the use of adhesive layer by merging the piezoelectric with the host structure through heat-treatment [36]: it is called direct bonding.

For this project, direct bonding is not practicable. The piezoelectric plates are glued to the surface using conductive epoxy. In order to prevent strong interface effects, the layer of glue has to be as thin as possible. Yet surface roughness would increase the thickness of the layer. As a consequence, the bottom surface of the bladed rail was smoothed with sandpaper. The surface treatment was hand-made, which lead to an irregular result (presence of very small hills).

The manual application of the glue is another issue: the layer should be thin and uniformly spread under the patches, which is very complicated to reach in practice. There is therefore an irregular bonding.

Finally, the shaping of the piezoelectric also presents some difficulties. The piezoelectric patches are obtained from bigger patches cut by half. The cut is not perfectly straight, which means the piezoelectric patch is not perfectly rectangular, possibly affecting the transducer's response.

5.2.3 External excitation

As mentioned in Chapter 1, the main external excitation on the blades of blisks are aerodynamics forces. To verify the performance of a damping system experimentally, we should prove it mitigates the effect of such excitation. This kind of excitation however is complicated to create and to control in a laboratory.

The simulation modelled this excitation by applying an unidirectional force on a point of the tip of each blade. The resulting displacement of the blade is then measured on the same point. Experimentally, measuring the displacement on one point without interacting with the system is easy to achieve using a laser vibrometer. Reproducing the exact same excitation is much more complicated because it tends to modify the system.

There are several methods used to excite bladed disks modes, such as: mechanical excitation by an electromagnetic shaker [37] or hammer impacts [13], electromagnetic excitation using multiple electromagnets [2] [13]. All those techniques alter the initial structure in some way: adding mass (attaching the magnets, the shaker), increasing structural damping (voice coil), inserting nonlinearity (by contact), introducing new resonances.

The experimental setup proposed in [2] to excite a blisk is shown on Figure 5.3 (a). The advantage of employing voice coils to excite punctually the blades is that it corresponds to the simulation and it constitutes a contactless method (thus avoiding nonlinear excitation). The frequency of the excitation can be controlled (contrasting with hammers). Having said that, the electromagnet system adds inherent damping to the structure which could be a problem to isolate the effect of the piezoelectric damping.

On Figure 5.3 (b), we show the picture of an experimental setup intent on the bladed rail using a piezoelectric stack as a shaker to excite the structure. This easy to implement solution does not allow to drive directly blades, as it is attached to the support. In this project, ideally, we would like to observe how well can piezoelectrics mounted on the support damp the blades when these are excited. This setup excites the structure from the support, which de facto is another situation. Besides, the clamped border conditions in this setup are not respected, the support becoming less stiff and thus separating more the modes of the first family (see Chapter 2).

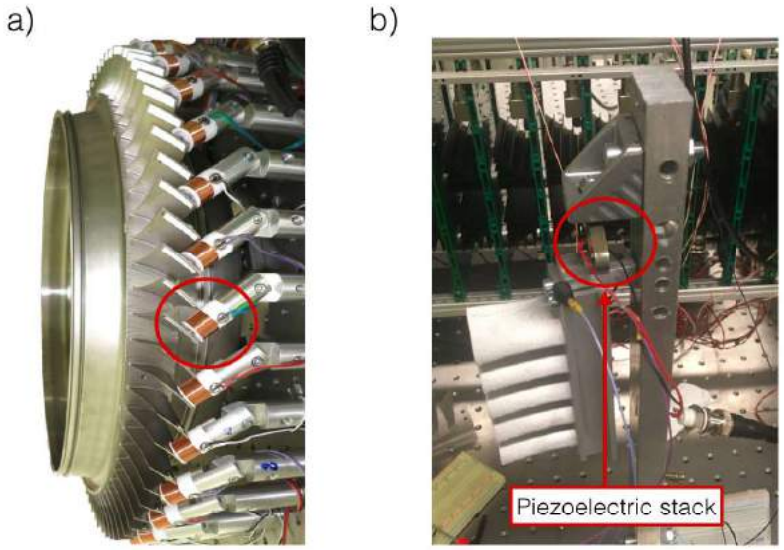

Figure 5.3 – (a) Experimental setup with voice coils [2]. The blades of the blisk of excited punctually with electromagnets. (b) Experimental setup created with a piezoelectric stack as electromechanical shaker. The bladed rail is attached to the shaker at its support.

The present work does not study experimentally the implementation of the piezoelectric damping systems, but it will be the first step of future investigations. The question of external excitation will then need to be answered acknowledging and evaluating the alterations they provoke on the bladed rail dynamics.

5.3 Method

The first objective of the experiments is to corroborate the simulation model validity. To that end, the configuration (a) of Figure 4.5 is replicated, with the difference that the bladed rail used is made of aluminium (AlSi10Mg) instead of steel, and the piezoelectric patches are composed of PIC151 (see Table 5.2 for material properties) instead of PIC255. The aluminium is indeed cheaper and its surface is easier to smooth manually, see Section 5.2.2. Regarding the piezoelectric material, the decision only relies on product availability. A comparison between the initial simulation setup and the experimental setup reproduced in simulation is proposed in Appendix C).

Pictures of the experimental setup are presented on Figure 5.4. Ten PIC151 patches are glued on the bottom surface of the support with epoxy conductive glue, acting as sensors and actuators. Thereby the bottom electrodes of the patches are all electrically connected to the bladed rail, itself connected to the ground. Cables are soldered on the top

Material property	Value	Unit
d_{31}	-180	$10^{-12}m/V$
d_{33}	400	$10^{-12}m/V$
d_{15}	550	$10^{-12}m/V$
S_{11}	15.0	$10^{-12}m^2/N$
S_{33}	19.0	$10^{-12}m^2/N$
S_{12}	-4.50	$10^{-12}m^2/N$
S_{13}	-5.70	$10^{-12}m^2/N$
S_{44}	39.0	$10^{-12}m^2/N$
e^{σ}_{11}	1.75	$10^{-8}F/m$
e^{σ}_{33}	2.12	$10^{-8}F/m$
ρ (density)	7800	kg/m^3

Table 5.2 – PIC151 material properties [8]. Physical meaning of the parameters explained in Section 1.2.1.

electrodes. The glue is thick and tricky to apply. As the piezoelectric transducers are very thin, the glue could touch both the bottom and the top electrodes of one patch, generating a short-circuit. It is the case of the sensor patch of pair 2, that is therefore useless.

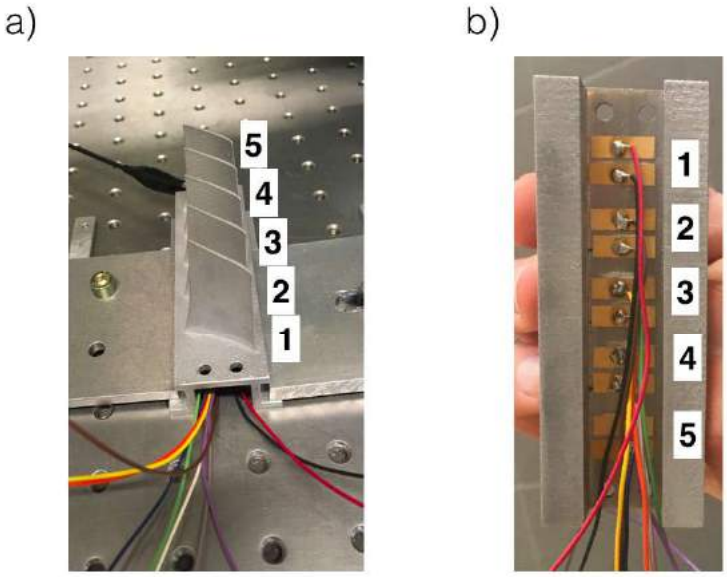

Figure 5.4 – Picture of the experimental setup used to obtain the transfer functions of V_{si}/V_{ai}. (a) The bladed rail is clamped by its feet to an optical table. A black cable (behind blade 5) connects the bladed rail to the ground. (b) Five piezoelectric pairs are glued with conductive epoxy of the bottom surface. For each patch, one electrode is connected to the ground through the bladed rail, the other one is linked to the MicroLabBox. Pair 2 is short-circuited because of a misapplication of the conductive glue, and is thus unusable.

In order to obtain the empirical transfer functions of V_{si}/V_{ai} (actuator patch voltage to sensor patch voltage of a pair i), input sine signals are sent to the actuator patches and output signals are collected at the sensor patches. A MicroLabBox allows to both generate the harmonic signals and to manage the sensor outputs.

Sine sweeps are executed for a duration of about 10 mins between 1100 Hz and 1400 Hz. The signals are measured with a sampling frequency of 10 kHz. From those experiments

results, the transfers functions V_{si}/V_{ai} are computed.

Equation 4.2, giving the expression of the transfer functions between actuator and sensor for lightly damped structure, can be factorised. Applying it to V_{si}/V_{ai}, we obtain [26]:

$$\frac{V_{si}}{V_{ai}}(s) = G_0 \frac{\prod_{k=1}^{N_z} s^2 + 2\xi_k \Omega_k + \Omega_k^2}{\prod_{l=1}^{N_p} s^2 + 2\xi_l \omega_l + \omega_l^2} \tag{5.1}$$

where N_z is the number of zeros, Ω_k are the frequencies of the zeros; N_p is the number of poles, ω_l are the frequencies of the poles; ξ_j is the modal damping of mode j; G_0 is the static gain.

This equation is used to fit the experimental curves and achieve empirical models. These models are then used to tune active damping technique parameters. As the effect of the patches on the blades is unknown (more experiments are needed), a first attempt to an active design vibration absorber is executed optimising its parameters by maximising the modal damping.

5.4 Results and discussion

The results of the frequency sweeps are displayed in Figure 5.5. The empirical transfer functions are exhibiting clear peaks at the natural frequencies, that can be extracted from those curves, see Table 5.3. The frequencies for each mode vary by 5 to 10 Hz depending on piezoelectric pair, impeding to define with clarity the correct natural frequencies.

Pair number	Frequency 1	Frequency 2	Frequency 3	Frequency 4	Frequency 5
1	1276.04 Hz	1290.21 Hz	1296.15 Hz	1300.72 Hz	-
3	1279.40 Hz	1294.07 Hz	1300.04 Hz	1304.16 Hz	1309.05 Hz
4	1271.17 Hz	1286.06 Hz	1291.99 Hz	1296.24 Hz	1300.64 Hz
5	1279.25 Hz	1294.07 Hz	1299.88 Hz	1304.32 Hz	1308.90 Hz

Table 5.3 – Experimental natural frequencies

The empirical models parameters are found, providing the modal damping ratios, see in Table 5.4. While in the simulations, the structural damping was assumed to be $\xi = 10^{-5}$, the modal damping ratios obtained from the experiments are located between $\xi_k = 10^{-4}$ and $\xi_k = 10^{-3}$ (for mode k), which is 10 to 100 times higher.

Pair number	ξ_1	ξ_2	ξ_3	ξ_4	ξ_5
1	$7.96\ 10^{-4}$	$5.00\ 10^{-4}$	$3.49\ 10^{-4}$	$1.17\ 10^{-3}$	-
3	$9.10\ 10^{-4}$	$5.00\ 10^{-4}$	$3.49\ 10^{-4}$	$3.50\ 10^{-4}$	$4.67\ 10^{-4}$
4	$1.71\ 10^{-3}$	$5.00\ 10^{-4}$	$3.49\ 10^{-4}$	$5.26\ 10^{-4}$	$2.92\ 10^{-4}$
5	$1.93\ 10^{-3}$	$5.00\ 10^{-4}$	$3.49\ 10^{-4}$	$2.34\ 10^{-4}$	$2.92\ 10^{-4}$

Table 5.4 – Experimental modal damping ratios

In the simulations, one of the biggest issues we were confronted to was the uncertain position of the first zero. Those result are showing more complex behaviour: depending of the piezoelectric pair, the system exhibits (1) a zero before pole pattern (see Fig. 5.5(b)) as in the simulation, (2) a pole before zero pattern (see Fig. 5.5(c) and (d)), or (3) a non-collocated system. Besides the zero before pole pattern behaviour is not completely caught by Eq. 5.1 as the first zero seems to be a positive zero (see the phase variation).

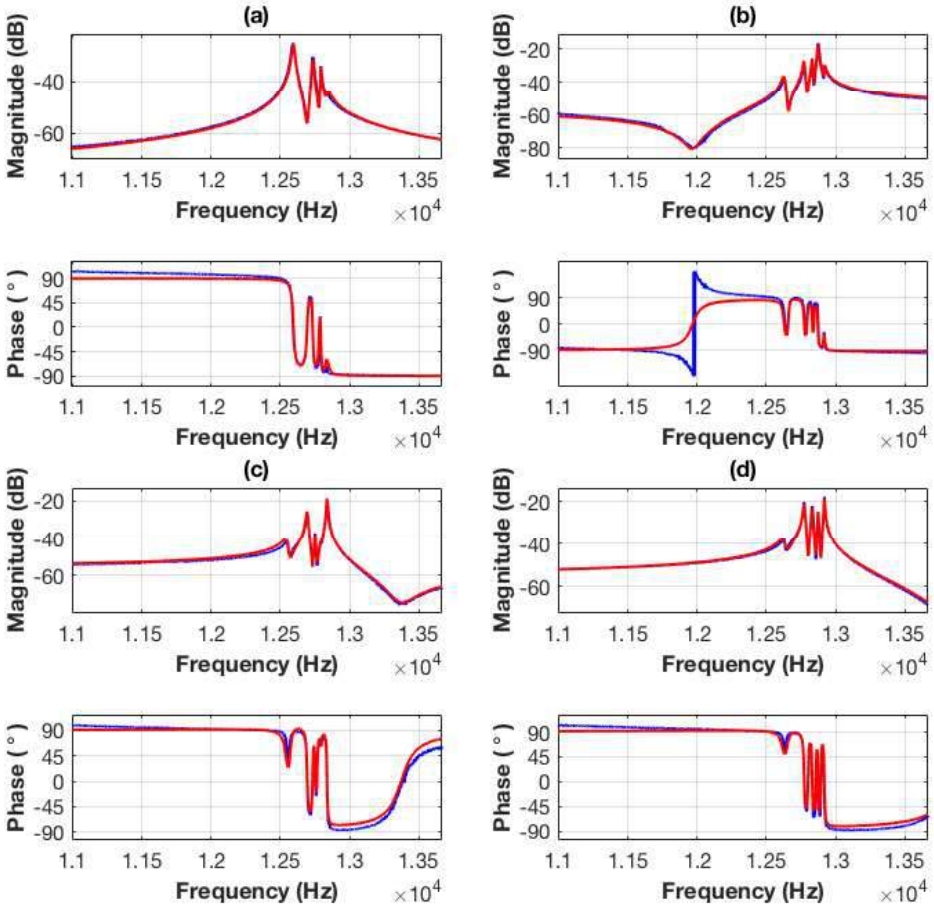

Figure 5.5 – Empirical transfer functions V_{si}/V_{ai} (blue curve) and the fitted model (red curve). (a) corresponds to pair 1; (b) pair 3; (c) pair 4; (d) pair 5. In the case of (d), a zero was added to the model in order to fit the experimental curve even if it was not confirmed as it would located out of the experimental frequency range.

These variations between the transfer functions could be explained by the imperfections of the setup (imperfect bonding or shape, etc., see Section 5.2.2) and seem to indicate that the position of the first zero is very sensitive.

The transfer functions are located between $-90°$ and $+90°$ instead of between $0°$ and $180°$. The models were adapted shifting their phase of $90°$. This difference could be due to the measuring electronics (some capacitance) or to a sampling effect.

The damping strategies developed so far are to be adapted to suit this new situation. The resonant controller (Negative Position Feedback) studied in Chapter 4 is still valid for the zero before pole transfer function. For the others, the Positive Position Feedback can be adopted, simply changing the sign of the loop of the NPF controller. Acting likewise feedback loops can be designed with identical parameters but different signs according to the piezoelectric pair. This was performed, optimising the parameters to provide maximum damping. The result is shown on Figure 5.6.

The result is promising: the modal damping ratios reach in average 3.2 10^{-3}. Never-

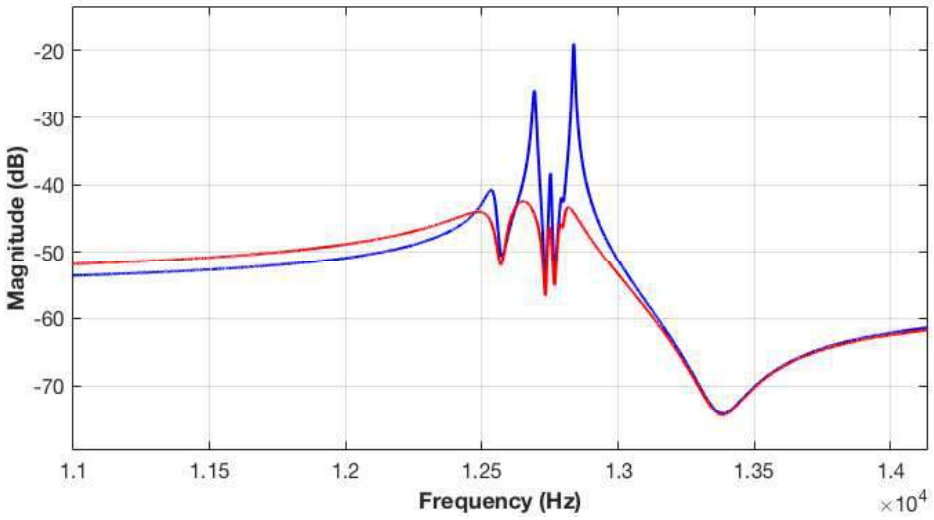

Figure 5.6 – Effect of PPF control on pair 4 transfer function. The parameters were chosen maximising modal damping of all four pairs transfer functions; the parameters are: $g = 3.5090\ 10^9$, $\omega_f = 8700.8$, $\xi_f = 0.1486$.

theless there are still many unknowns. Firstly, in this model, there is no coupling between the piezoelectric pairs, which of course is inaccurate. The coupling needs to be acknowledged for damper designs in terms of performance but also in terms of stability robustness. Secondly, the damping performance can not really be predicted without determining the influence of the patches on the blades and vice-versa, which requires further experiments.

5.5 Conclusion

An aluminium prototype of the bladed rail was 3D printed, on which piezoelectric plates were mounted, reproducing the configuration proposed in Figure 4.5 (a). The main objective was to obtain the empirical transfer functions between the actuators and the sensors voltages for each piezoelectric pairs (V_{si}/V_{ai} for pair i).

Those transfer functions were measured by frequency sweeps. They present several natural frequency values for a same mode and exhibit different behaviours in terms of zero pole interlacing patterns. Those variations could be due to many reasons, such as imperfect piezoelectric placement, shaping or surface bonding. The quality of the bladed rail bottom surface also could cause such deviations, as it was unevenly smoothed manually.

Despite this, the sharp peaks of the transfer functions, meaning the piezoelectric patches actually interact with the structure, suggest that damping is possible. Empirical models were created and a resonant controller was applied to them.

Even if the results are promising, further experiments are required to complete the model in order to include coupling between the patches pairs and between the pairs and the blades.

Finally, the vibration absorber will need to be applied to the prototype with an external excitation in order to evaluate its real performance. The external excitation must be carefully selected, taking into account the effect of its implementation on the primary structure dynamics.

Chapter 6
Conclusion

The present thesis investigated the application of piezoelectric damping devices on a blisk-like structure: the bladed rail. The main idea was to reduce blade vibrations by operating on the support bottom surface, where modifications can be made without affecting the rail upper part which possesses an aerodynamic function. While other damping techniques exist, the ones proposed in this work are easy-to-implement and non-intrusive, as it consists in simply attaching piezoelectric patches on a surface. Those transducers are then connected to circuits, used as actuator/sensor in order to create effective dampers.

Operating from the bottom surface to damp the blades is possible, as there is an interaction between those two sub-structures. The motion of the blades lead to strains of the surface underneath that are in phase with that motion. We saw that the bladed rail, as any periodic structure, exhibits a succession of closely located natural frequencies, corresponding to family of modes. The first family, situated at around 1.2 kHz, is composed of five modes in which the blades are found in their first bending mode. The objective set for this study was to specifically reduce the vibration related to those modes.

The piezoelectric transducers were placed at the root of the blades, where they could adequately control them. Mokrani (2015), in his PhD thesis [2], proposed to place five patches under each blade and to shunt them with identical RL circuits, tuned on the mean frequency of the first family of modes. His optimisation algorithm was confronted to an H_∞ approach that showed better performance in terms of vibration reduction. Electrical component mistuning on this kind of resonant shunt creates high loses of performance and is one of the limiting factors of the method.

Active damping techniques were then developed. Five pairs of sensor and actuator patches were mounted on the bottom surface. The pairs were chosen to show a collocated behaviour, which ensures the stability of well-known control methods. In this case, an integral control and two negative position feedback controls (resonant controls) were implemented. The resonant controller has the best performance but its low stability robustness is a strong disadvantage. When its robustness is increased, its performances decreases. Integral control, on the other hand, exhibits very convincing performance, keeping also a good robustness. Moreover, the control is broadband and not only affects the first family of modes.

The results of this work can be summarised by the performance graph on figure 6.1, where the mean RL shunt, the optimal RL shunt, the integral control and the resonant control are compared.

This study achieved the goal to propose strategies that show better performance than the approach that Mokrani (2015) worked on (mean RL shunt). Based on our results, the selection of the best damping strategy lies on several criteria. If high performance is required, the resonant active damping is better suited. However, its lack of robustness can be problematic for its practical implementation. With a similar performance, the RL shunt and the integral control both have advantages and disadvantages. The RL shunt is a passive technique that, by definition, does not need external power source. But it only damps the first family of modes and is sensitive to mistuning. The integral control, on

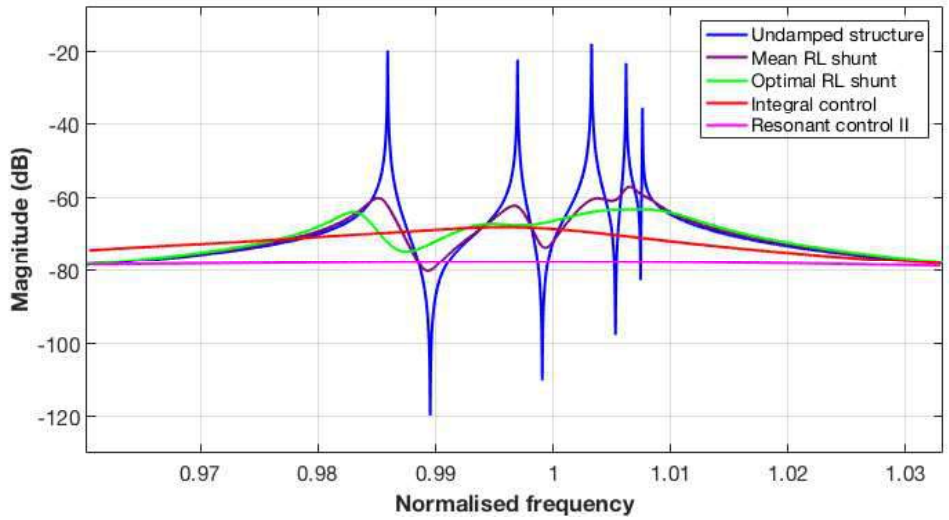

Figure 6.1 – Damping performance of the different approaches investigated. Transfer function X_1/F_1.

the other hand, requires external power source, but shows good stability robustness and is efficient broadband. As a conclusion, the choice of a method over another derives from those considerations according to one's constraints.

On the simulation side, there is still a lot of space for improvement. Some phenomena were not completely studied in this work and an some deepening would be extremely interesting: the problem of the mesh depending zero position in the sensor/actuator transfer function, the effect of the piezoelectric patches thickness of damping performance, the modelling of indirect bonding. Besides, passive and active damping techniques are not the only options available. The next steps of this investigation should address hybrid damping and energy harvesting.

On the experimental side, a prototype of the bladed rail was 3D-printed in order to test the active damping configuration. The transfer functions between the sensors and actuators were obtained and a model was created. Resonant shunt was applied on this model, showing the potential of the technique. The experiments exhibited many challenges, such as surface roughness, piezoelectric imperfect bonding or excitation source. Many more experiments are needed to better understand the system behaviour and to assess the damping approaches developed in the simulations. This should constitute the very next steps for the continuation of this project.

Bibliography

[1] B. Zhou, "Etude de l'amortissement piézoélectrique shunté appliqué aux roues aubagées désaccordées," Ph.D. dissertation, 2012.

[2] B. Mokrani, "Piezoelectric shunt damping of rotationally periodic structures," Ph.D. dissertation, Ph. D. Thesis, Université Libre de Bruxelles, Active Structures Laboratory ..., 2015.

[3] S. R. Moheimani and A. J. Fleming, *Piezoelectric transducers for vibration control and damping*. Springer Science & Business Media, 2006.

[4] J. J. Wijker, *Spacecraft structures*. Springer Science & Business Media, 2008.

[5] E. Balmes and A. Deraemaeker, "Modeling structures with piezoelectric materials," *SDT tutorial*, 2013.

[6] K. Kempen, L. Thijs, J. Van Humbeeck, and J.-P. Kruth, "Mechanical properties of alsi10mg produced by selective laser melting," *Physics Procedia*, vol. 39, pp. 439–446, 2012.

[7] J. Wu, L. Wang, and X. An, "Numerical analysis of residual stress evolution of alsi10mg manufactured by selective laser melting," *Optik*, vol. 137, pp. 65–78, 2017.

[8] S. Moharana, "Modelling of piezo-structure elastodynamic interaction through bond layer for electro-mechanical impedance technique," Ph.D. dissertation, 2012.

[9] B. Mokrani, R. Bastaits, R. Viguié, and A. Preumont, "Vibration damping of turbomachinery components with piezoelectric transducers: Theory and experiment," in *ISMA2012 International Conference on Noise and Vibration Engineering, Leuven, Belgium*, vol. 69, 2012.

[10] A. Rittweger, J. Albus, E. Hornung, H. Öry, and P. Mourey, "Passive damping devices for aerospace structures," *Acta Astronautica*, vol. 50, no. 10, pp. 597–608, 2002.

[11] A. S. Rangwala, *Turbo-machinery dynamics*. McGraw-Hill,, 2005.

[12] E. Petrov and D. Ewins, "Effects of damping and varying contact area at blade-disk joints in forced response analysis of bladed disk assemblies," 2006.

[13] Y. J. Chan, "Variability of blade vibration in mistuned bladed discs," Ph.D. dissertation, Imperial College London (University of London), 2009.

[14] E. Balmes, M. Corus, S. Baumhauer, P. Jean, and J.-P. Lombard, "Constrained viscoelastic damping, test/analysis correlation on an aircraft engine," in *Structural Dynamics, Volume 3*. Springer, 2011, pp. 1177–1185.

[15] Y. Chen, J. Zhai, and Q. Han, "Vibration and damping analysis of the bladed disk with damping hard coating on blades," *Aerospace Science and Technology*, vol. 58, pp. 248–257, 2016.

[16] J. Laborenz, M. Krack, L. Panning, J. Wallaschek, M. Denk, and P.-A. Masserey, "Eddy current damper for turbine blading: electromagnetic finite element analysis and measurement results," *Journal of engineering for gas turbines and power*, vol. 134, no. 4, 2012.

[17] J. L. Kauffman, "Vibration reduction of integrally bladed rotors using piezoelectric materials," 2012.

[18] P. Shivashankar and S. Gopalakrishnan, "Review on the use of piezoelectric materials for active vibration, noise, and flow control," *Smart Materials and Structures*, 2020.

[19] B. Yan, K. Wang, Z. Hu, C. Wu, and X. Zhang, "Shunt damping vibration control technology: A review," *Applied Sciences*, vol. 7, no. 5, p. 494, 2017.

[20] K. Marakakis, G. K. Tairidis, P. Koutsianitis, and G. E. Stavroulakis, "Shunt piezoelectric systems for noise and vibration control: A review," *Frontiers in Built Environment*, vol. 5, p. 64, 2019.

[21] A. Paknejad, G. Raze, G. Zhao, M. Osée, A. Deraemaeker, F. Robert, G. Kerschen, and C. Collette, "Hybridization of active control and passive resonant shunt."

[22] A. Paknejad, G. Rahimi, A. Farrokhabadi, and M. M. Khatibi, "Analytical solution of piezoelectric energy harvester patch for various thin multilayer composite beams," *Composite structures*, vol. 154, pp. 694–706, 2016.

[23] T. M. P. Silva and C. De Marqui, "Self-powered active control of elastic and aeroelastic oscillations using piezoelectric material," *Journal of Intelligent Material Systems and Structures*, vol. 28, no. 15, pp. 2023–2035, 2017.

[24] H. Liu, J. Zhong, C. Lee, S.-W. Lee, and L. Lin, "A comprehensive review on piezoelectric energy harvesting technology: Materials, mechanisms, and applications," *Applied Physics Reviews*, vol. 5, no. 4, p. 041306, 2018.

[25] D. Laxalde, F. Thouverez, and J.-P. Lombard, "Forced response analysis of integrally bladed disks with friction ring dampers," *Journal of Vibration and Acoustics*, vol. 132, no. 1, 2010.

[26] A. Preumont, *Vibration control of active structures: an introduction*. Springer, 2011, vol. 246.

[27] A. Rittweger, J. Albus, E. Hornung, H. Öry, and P. Mourey, "Passive damping devices for aerospace structures," *Acta Astronautica*, vol. 50, no. 10, pp. 597–608, 2002.

[28] C. Hansen, S. Snyder, X. Qiu, L. Brooks, and D. Moreau, *Active control of noise and vibration*. CRC press, 2012.

[29] C. Collette, "Lecture notes in active structures," 2020.

[30] N. Lobontiu, *System dynamics for engineering students: Concepts and applications*. Academic Press, 2017.

[31] B. Denkena, *New Production Technologies in Aerospace Industry: Proceedings of the 4th Machining Innovations Conference, Hannover, September 2013*. Springer Science & Business Media, 2013.

[32] C. Y. Yap, C. K. Chua, Z. L. Dong, Z. H. Liu, D. Q. Zhang, L. E. Loh, and S. L. Sing, "Review of selective laser melting: Materials and applications," *Applied physics reviews*, vol. 2, no. 4, p. 041101, 2015.

[33] C. Jin and X. Wang, "Analytical modelling of the electromechanical behaviour of surface-bonded piezoelectric actuators including the adhesive layer," *Engineering Fracture Mechanics*, vol. 78, no. 13, pp. 2547–2562, 2011.

[34] L. Han, X. Wang, and Y. Sun, "The effect of bonding layer properties on the dynamic behaviour of surface-bonded piezoelectric sensors," *International Journal of Solids and Structures*, vol. 45, no. 21, pp. 5599–5612, 2008.

[35] O. Rabinovitch and J. R. Vinson, "Adhesive layer effects in surface-mounted piezoelectric actuators," *Journal of intelligent material systems and structures*, vol. 13, no. 11, pp. 689–704, 2002.

[36] K. Eda, K. Onishi, H. Sato, Y. Taguchi, and M. Tomita, "Direct bonding of piezoelectric materials and its applications," in *2000 IEEE Ultrasonics Symposium. Proceedings. An International Symposium (Cat. No. 00CH37121)*, vol. 1. IEEE, 2000, pp. 299–309.

[37] D. Laxalde, F. Thouverez, J.-J. Sinou, J.-P. Lombard, and S. Baumhauer, "Mistuning identification and model updating of an industrial blisk," *International Journal of Rotating Machinery*, vol. 2007, 2007.

Appendix A

Material effect on dynamics

Modifying the material properties of the 3D model result in different resonance frequencies. However the mode shapes and the mode families structure stay valid. When the frequencies are normalised, we can observe that the material does not matter anymore, as shown in Table A.1. This is why, in this study, most of the graphs are presented with normalised frequencies.

-	Titanium	Steel	Aluminium
Natural frequency 1	1193.7 Hz	1237.3 Hz	1216.5 Hz
Natural frequency 2	1206.9 Hz	1251.0 Hz	1230.0 Hz
Natural frequency 3	1215.0 Hz	1259.2 Hz	1238.2 Hz
Natural frequency 4	1218.3 Hz	1262.9 Hz	1241.7 Hz
Natural frequency 5	1219.9 Hz	1264.6 Hz	1243.3 Hz
Mean frequency	1210.8 Hz	1255.0 Hz	1233.9 Hz
Normalised frequency 1	0.9859	0.9859	0.9859
Normalised frequency 2	0.9968	0.9968	0.9968
Normalised frequency 3	1.0035	1.0033	1.0035
Normalised frequency 4	1.0062	1.0063	1.0063
Normalised frequency 5	1.0075	1.0076	1.0076
Standard deviation	0.0089	0.0089	0.0089

Table A.1 – Natural frequencies of the first family of modes for different materials (metals) from simulations. The normalised frequencies are computed by dividing the natural frequencies by the mean frequency.

Appendix B

Active configuration comparison

In chapter 4, the patch configurations are presented and the configuration (a) is selected over configuation (b) (see Fig. 4.5). The figure B.1 justifies that choice. For the same optimisation algorithm - damping maximisation - the configuration (a) exhibits far better results than configuration (b) in terms of peak reduction.

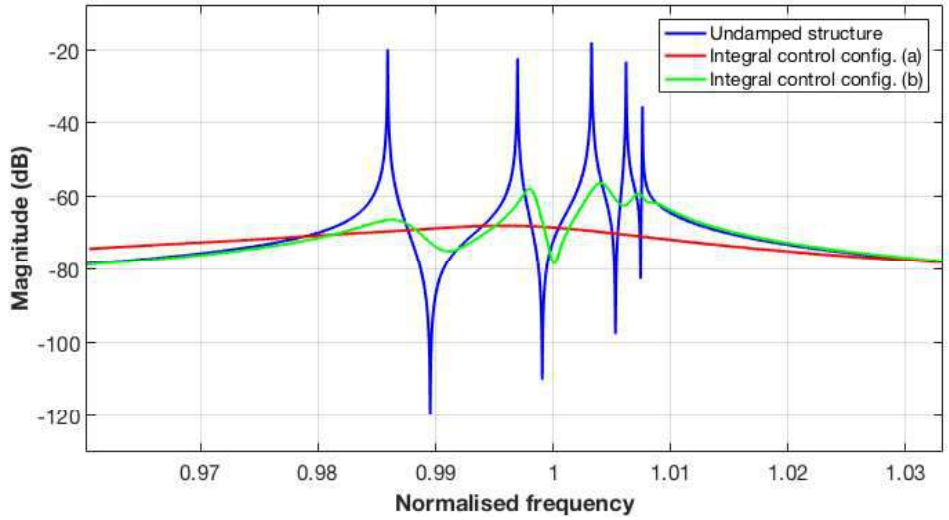

Figure B.1 – Damping performance of optimised integral control for config. (a) and (b) of Fig. 4.5. Transfer function X_1/F_1.

Appendix C

Experimental setup in simulations

In the present work, the simulations were completed using the steel mechanical characteristics and PIC255 piezoelectric patches. The experiments, on the other hand, consist in employing an aluminium prototype on which are glued PIC151 piezoelectrics. Moreover, the clamped boundary conditions are different in the two situations: in the simulation, the rail is clamped at the holes, while in the experiment, the rail feet are blocked.

As explained in Appedix A, changing the material of the same model does not modify the normalised frequencies. The natural frequencies stay in the same range of magnitude. However, as shown in Figure C.1, we observe that the frequencies of the experimental setup model are located closer to each other than the frequencies of the simulation setup model. It is because clamping the feet make the bladed rail support even stiffer. Therefore the natural frequencies are found in a more narrow band.

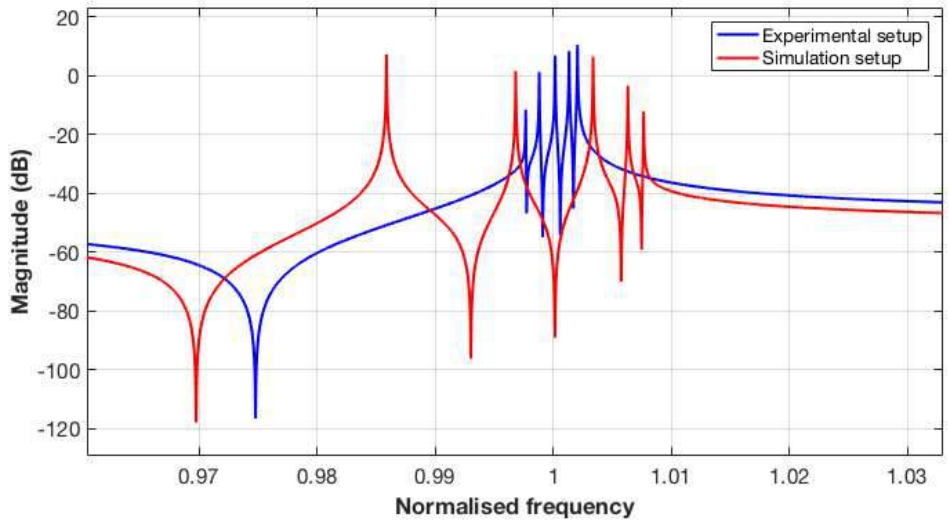

Figure C.1 – Transfer function V_{s1}/V_{a1} from SDT simulation. In blue, the model adapted to the experimental setup (Aluminium, PIC151 patches and feet clamped), in red the simulation configuration used in the chapter 4.

In Figure C.2, the experimental results and the simulation results of the experimental setup model are compared. One can see three main differences: (1) there is no zero before pole in the experimental results; (2) the frequencies are higher in the experiments; and (3) the amplitude of the peaks is lower.

The point (1) is discussed in Chapter 5. In the case of point (2), the system is different: the real boundary conditions, the 3D printed material, might make the support even stiffer. (3) The difference of amplitude is probably mainly due to the inherent damping of the simulation model that is largely underestimated. The imperfect bonding of the patches in the real structure could also provoke such variation.

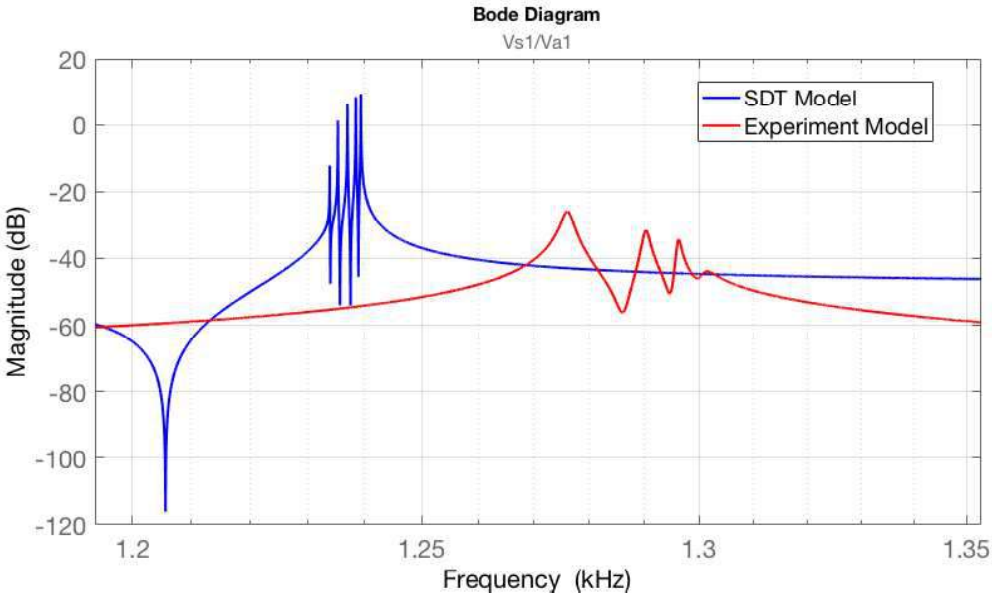

Figure C.2 – Transfer function V_{s1}/V_{a1}. In blue, the SDT model adapted to the experimental setup. In red, the model fitted on the experimental results.

Appendix D

Matlab Codes

D.1 Five patches SDT model generation

The code is used to import abaqus files and generate a State Space model of the five patches bladed rail model from Chapter 3.

```
clear all
clc

model = abaqus('blaidedrail_abaqus_model.inp');
model2 = model.Stack{2,3};
model2.Node(:,5:7) = model2.Node(:,5:7)/1000; model2.unit = 'SI';
    % changing units

model2.name = 'Bladed Rail - Passive shunt - Mokrani like model';

% Defining a group corresponding to piezo patches
  model2.Elt = feutil(['divide group 1 withnode{x<0.027 & x>0.011
      & y<-0.0115 & y>-0.0225 & z>0.0145 & z<0.015}'],model2);
  model2.Elt = feutil(['divide group 2 withnode{x<0.027 & x>0.011
      &  y<-0.028 & y>-0.039 & z>0.0145 & z<0.015}'],model2);
  model2.Elt = feutil(['divide group 3 withnode{x<0.027 & x>0.011
      &  y<-0.0445 & y>-0.0555 & z>0.0145 & z<0.015}'],model2);
  model2.Elt = feutil(['divide group 4 withnode{x<0.027 & x>0.011
      & y<-0.061 & y>-0.072 & z>0.0145 & z<0.015}'],model2);
  model2.Elt = feutil(['divide group 5 withnode{x<0.027 & x>0.011
      & y<-0.0775 & y>-0.0885 & z>0.0145 & z<0.015}'],model2);

  model2.Elt=feutil('set group 1 matid 2',model2);
  model2.Elt=feutil('set group 2 matid 2',model2);
  model2.Elt=feutil('set group 3 matid 2',model2);
  model2.Elt=feutil('set group 4 matid 2',model2);
  model2.Elt=feutil('set group 5 matid 2',model2);
  model2.Elt=feutil('set group 6 matid 1',model2);

% Adding material properties
model2.pl = [1 fe_mat('m_elastic','SI',1) 205e9 0.3 7800 0 0 0
    0];% <- steel
model2.pl = m_piezo(model2.pl,'dbval 2 -elas 20 PIC_255'); %
    Selecting piezo material

% Adding element properties
model2 = p_solid('default',model2);
```

```
30
31 %% ADD CASE
32 % RESET CASE 1
33 model2 = fe_case(model2,'reset') ;
34
35 % SET THE
36 [Case,CaseName]=fe_case(model,'GetCase') ;
37 model2 = fe_case(model2,'SetCase',Case) ;
38 model2 = stack_set(model2,stack_get(model,'case'));
39
40 % Adding the boundary condition
41 % GET THE SET7 BY NODE ID   -   Set 7 is defined in abaqus as
       such
42 % avoid to have multiple succesive selection rules...
43 Set7 = stack_get(model,'set','Set-7');
44 Set7{3}.data = feutil('findnode setname Set-7',model);
45 model2 = stack_set(model2,Set7);
46
47
48
49 %% Considering voltage actuator and charge sensor
50 % Patch1
51    model2 = p_piezo('ElectrodeMPC Top1 Actuator -input "Va"',
          model2,'x<0.027 & x>0.011 & y<-0.0115 & y>-0.0225 & z
          ==0.0145');
52    model2 = p_piezo('ElectrodeMPC Bottom1 Actuator -ground',model2
          ,'x<0.027 & x>0.011 & y<-0.0115 & y>-0.0225 & z==0.015');
53
54    N1 = feutil('find node x<0.027 & x>0.011 & y<-0.0115 & y
          >-0.0225 & z==0.0145',model2);
55    N1 = N1(1);
56    r1 = struct('cta',1,'DOF',N1+.21,'name','QS1');
57    model2 = p_piezo('ElectrodeSensQ',model2,r1);
58
59 % Patch2
60    model2 = p_piezo('ElectrodeMPC Top2 Actuator -input "Va"',
          model2,'x<0.027 & x>0.011 &  y<-0.028 & y>-0.039 & z==0.0145
          ');
61    model2 = p_piezo('ElectrodeMPC Bottom2 Actuator -ground',model2
          ,'x<0.027 & x>0.011 &  y<-0.028 & y>-0.039 & z==0.015');
62
63    N2 = feutil('find node x<0.027 & x>0.011 &  y<-0.028 & y>-0.039
           & z==0.0145',model2);
64    N2 = N2(1);
65    r2 = struct('cta',1,'DOF',N2+.21,'name','QS2');
66    model2 = p_piezo('ElectrodeSensQ',model2,r2);
67
```

```
68 % Patch3
69   model2 = p_piezo('ElectrodeMPC Top3 Actuator -input "Va"',
         model2,'x<0.027 & x>0.011 &  y<-0.0445 & y>-0.0555 & z
         ==0.0145');
70   model2 = p_piezo('ElectrodeMPC Bottom3 Actuator -ground',model2
         ,'x<0.027 & x>0.011 &  y<-0.0445 & y>-0.0555 & z==0.015');
71
72   N3 = feutil('find node x<0.027 & x>0.011 &  y<-0.0445 & y
         >-0.0555 & z==0.0145',model2);
73   N3 = N3(1);
74   r3 = struct('cta',1,'DOF',N3+.21,'name','QS3');
75   model2 = p_piezo('ElectrodeSensQ',model2,r3);
76
77 % Patch4
78   model2 = p_piezo('ElectrodeMPC Top4 Actuator -input "Va"',
         model2,'x<0.027 & x>0.011 & y<-0.061 & y>-0.072 & z==0.0145'
         );
79   model2 = p_piezo('ElectrodeMPC Bottom4 Actuator -ground',model2
         ,'x<0.027 & x>0.011 & y<-0.061 & y>-0.072 & z==0.015');
80
81   N4 = feutil('find node x<0.027 & x>0.011 & y<-0.061 & y>-0.072
         & z==0.0145',model2);
82   N4 = N4(1);
83   r4 = struct('cta',1,'DOF',N4+.21,'name','QS4');
84   model2 = p_piezo('ElectrodeSensQ',model2,r4);
85
86 % Patch5
87   model2 = p_piezo('ElectrodeMPC Top5 Actuator -input "Va"',
         model2,'x<0.027 & x>0.011 & y<-0.0775 & y>-0.0885 & z
         ==0.0145');
88   model2 = p_piezo('ElectrodeMPC Bottom5 Actuator -ground',model2
         ,'x<0.027 & x>0.011 & y<-0.0775 & y>-0.0885 & z==0.015');
89
90   N5 = feutil('find node x<0.027 & x>0.011 & y<-0.0775 & y
         >-0.0885 & z==0.0145',model2);
91   N5 = N5(1);
92   r5 = struct('cta',1,'DOF',N5+.21,'name','QS5');
93   model2 = p_piezo('ElectrodeSensQ',model2,r5);
94
95 % Merging Dofsets
96   data.def = [1 0 0 0 0;0 1 0 0 0;0 0 1 0 0;0 0 0 1 0;0 0 0 0
         1]';
97   data.DOF = [N1+0.21 N2+0.21 N3+0.21 N4+0.21 N5+0.21]';
98   model2 = fe_case(model2,'DofSet','Va',data);
99
100  % Excitation
101
```

```
% Blade 1
NF = 4861;      % The node is chosen to be on the tip of the blade
LoadCase = struct('DOF',NF+0.02,'def',1);
% Point Actuator
model2 = fe_case(model2,'DOFLoad','TipLoad1',LoadCase);

% Point Sensor
model2 = fe_case(model2,'SensDof','TipDisp1',NF+0.02);

% Blade 2
NF = 5300;
LoadCase = struct('DOF',NF+0.02,'def',1);
model2 = fe_case(model2,'DOFLoad','TipLoad2',LoadCase);

model2 = fe_case(model2,'SensDof','TipDisp2',NF+0.02);

% Blade 3
NF = 5739;
LoadCase = struct('DOF',NF+0.02,'def',1);
model2 = fe_case(model2,'DOFLoad','TipLoad3',LoadCase);

model2 = fe_case(model2,'SensDof','TipDisp3',NF+0.02);

% Blade 4
NF = 6171;
LoadCase = struct('DOF',NF+0.02,'def',1);
model2 = fe_case(model2,'DOFLoad','TipLoad4',LoadCase);

model2 = fe_case(model2,'SensDof','TipDisp4',NF+0.02);

% Blade 5
NF = 6617;
LoadCase = struct('DOF',NF+0.02,'def',1);
model2 = fe_case(model2,'DOFLoad','TipLoad5',LoadCase);

model2 = fe_case(model2,'SensDof','TipDisp5',NF+0.02);

%% Calculating the resonance frequencies and mode shapes
ofact('mklserv_utils -silent')
def = fe_eig(model2,[5 50 10]);
def.data

%% Creating state space model
model2 = stack_set(model2,'info','DefaultZeta',1e-5);
[sys,TR] = fe2ss('free 5 20 0 -dterm',model2);

%% Visualization
```

```
149 feplot(model2);
150 fecom('colordatapro')
```

D.2 10 patches SDT model generation

The code is used to import abaqus files and generate a State Space model of the ten patches bladed rail model from Chapter 4.

```
1  clear all
2  clc
3
4  model = abaqus('blaidedrail_abaqus_model.inp');
5
6  model2 = model.Stack{2,3};
7  model2.Node(:,5:7) = model2.Node(:,5:7)/1000; model2.unit = 'SI';
       % changing units
8
9  model2.name = 'Bladed Rail - Ten Patches - Configuration 19';
10
11 % Defining a group corresponding to piezo (actuators)
12    model2.Elt = feutil(['divide group 1 withnode{x<0.0255 & x
          >0.0105 & y<-0.01325 & y>-0.01825 & z>0.0148 & z<0.015}'],
          model2);
13    model2.Elt = feutil(['divide group 2 withnode{x<0.0255 & x
          >0.0105 &  y<-0.02975 & y>-0.03475 & z>0.0148 & z<0.015}'],
          model2);
14    model2.Elt = feutil(['divide group 3 withnode{x<0.0255 & x
          >0.0105 &  y<-0.04625 & y>-0.05125 & z>0.0148 & z<0.015}'],
          model2);
15    model2.Elt = feutil(['divide group 4 withnode{x<0.0255 & x
          >0.0105 & y<-0.06275 & y>-0.06775 & z>0.0148 & z<0.015}'],
          model2);
16    model2.Elt = feutil(['divide group 5 withnode{x<0.0255 & x
          >0.0105 & y<-0.07925 & y>-0.08425 & z>0.0148 & z<0.015}'],
          model2);
17
18 % Defining a group corresponding to piezo (sensors)
19    model2.Elt = feutil(['divide group 6 withnode{x<0.0255 & x
          >0.0105 & y<-0.01875 & y>-0.02375 & z>0.0148 & z<0.015}'],
          model2);
20    model2.Elt = feutil(['divide group 7 withnode{x<0.0255 & x
          >0.0105 &  y<-0.03525 & y>-0.04025 & z>0.0148 & z<0.015}'],
          model2);
21    model2.Elt = feutil(['divide group 8 withnode{x<0.0255 & x
          >0.0105 &  y<-0.05175 & y>-0.05675 & z>0.0148 & z<0.015}'],
          model2);
22    model2.Elt = feutil(['divide group 9 withnode{x<0.0255 & x
          >0.0105 & y<-0.06825 & y>-0.07325 & z>0.0148 & z<0.015}'],
```

```
        model2);
23    model2.Elt = feutil(['divide group 10 withnode{x<0.0255 & x
        >0.0105 & y<-0.08475 & y>-0.08975 & z>0.0148 & z<0.015}'],
        model2);
24
25
26
27
28 for i0=1:10
29
30      model2.Elt = feutil(sprintf('set group %i matid 2',i0),model2
          );
31
32 end
33
34    model2.Elt = feutil('set group 11 matid 1',model2);
35
36 % Adding material properties
37 model2.pl = [1 fe_mat('m_elastic','SI',1) 205e9 0.3 7800 0 0 0
      0];    % Steel
38 % Aluminium would be 70e9 0.30 2700
39
40 model2.pl = m_piezo(model2.pl,'dbval 2 -elas 20 PIC_255');  %
      Selecting piezo material
41
42 % Adding element properties
43 model2 = p_solid('default',model2);
44 % return
45 %% ADD CASE
46 % RESET CASE 1
47 model2 = fe_case(model2,'reset') ;
48
49 % SET THE
50 [Case,CaseName]=fe_case(model,'GetCase') ;
51 model2 = fe_case(model2,'SetCase',Case) ;
52 model2 = stack_set(model2,stack_get(model,'case'));
53
54 % Adding the boundary condition
55 % GET THE SET7 BY NODE ID    -    Set 7 is defined in abaqus as
      such
56 % avoid to have multiple succesive selection rules...
57 Set7 = stack_get(model,'set','Set-7');
58 Set7{3}.data = feutil('findnode setname Set-7',model);
59 model2 = stack_set(model2,Set7);
60
61 %% Considering voltage actuator and charge sensor
62
```

```
63 InputDOF = [];
64 GROUPa = [1 2 3 4 5];
65 GROUPs = [6 7 8 9 10];
66 zPOS   = [0.0148 0.015 ];
67
68 for i1=1:length(GROUPa)
69
70     [model2,InputDOF(end+1,1)] = p_piezo(sprintf('ElectrodeMPC
       Top%i Actuator -input "Va%i" ',GROUPa(i1),GROUPa(i1)) ,
       model2, sprintf('z==%f & inelt{group %i} ',zPOS(1),GROUPa
       (i1)));
71     model2 = p_piezo(sprintf('ElectrodeMPC Bottom%i Actuator -
       ground' ,GROUPa(i1),GROUPa(i1)) , model2, sprintf('z
       ==%f & inelt{group %i} ',zPOS(2),GROUPa(i1)));
72
73     model2 = p_piezo(sprintf('ElectrodeMPC Vs%i sensor -matid 2 -
       vout',GROUPa(i1)),model2,sprintf('z==%f & inelt{group %i}
        ',zPOS(1),GROUPs(i1)));
74     model2 = p_piezo(sprintf('ElectrodeMPC Bottom%i sensor -
       ground',GROUPs(i1)),model2,sprintf('z==%f & inelt{group %
       i} ',zPOS(2),GROUPs(i1)));
75     model2 = fe_case(model2,'remove',sprintf('Q-Vs%i sensor',
       GROUPa(i1)));
76
77     NAME{i1} = sprintf('Va%i' ,GROUPa(i1));
78
79 end
80
81 model2 =fe_mpc('DofSetMerge',model2,NAME{:}) ; % DOFset are
       groups under the name as NAME{1};
82 % return
83
84 % Excitation on the blades
85
86 % Blade 1
87 NF = 9881;   % The node is chosen to be on the tip of the blade
88
89 % Point Actuator Blade 1
90 LoadCase = struct('DOF',NF+0.02,'def',1);
91 model2 = fe_case(model2,'DOFLoad','TipLoad1',LoadCase);
92
93 % Point Sensor Blade 1
94 model2 = fe_case(model2,'SensDof','TipDisp1',NF+0.02);
95
96 % Blade 2
97 NF = 7953;
98 LoadCase = struct('DOF',NF+0.02,'def',1);
```

```
99 model2 = fe_case(model2,'DOFLoad','TipLoad2',LoadCase);
100
101 model2 = fe_case(model2,'SensDof','TipDisp2',NF+0.02);
102
103 % Blade 3
104 NF = 8169;
105 LoadCase = struct('DOF',NF+0.02,'def',1);
106 model2 = fe_case(model2,'DOFLoad','TipLoad3',LoadCase);
107
108 model2 = fe_case(model2,'SensDof','TipDisp3',NF+0.02);
109
110 % Blade 4
111 NF = 8385;
112 LoadCase = struct('DOF',NF+0.02,'def',1);
113 model2 = fe_case(model2,'DOFLoad','TipLoad4',LoadCase);
114
115 model2 = fe_case(model2,'SensDof','TipDisp4',NF+0.02);
116
117 % Blade 5
118 NF = 8601;
119 LoadCase = struct('DOF',NF+0.02,'def',1);
120 model2 = fe_case(model2,'DOFLoad','TipLoad5',LoadCase);
121
122 model2 = fe_case(model2,'SensDof','TipDisp5',NF+0.02);
123
124 %% Calculating the resonance frequencies and mode shapes
125  ofact('mklserv_utils -silent')
126  def = fe_eig(model2,[5 50 10]);
127  def.data
128
129 %% Creating state space model
130
131 model2 = stack_set(model2,'info','DefaultZeta',1e-5);
132 [sys,TR] = fe2ss('free 5 20 0 -dterm',model2);
133
134 return
135 %% Visualization
136 feplot(model2);
137 fecom('colordatapro')
```

D.3 Mean shunt appoach algorithm

The code generates the shunted state space model of the bladed rail from a five patches model, choosing the parameters with the mean shunt approach.

```
1 load('system_with_five_patches.mat') ;    % loading state space
    model with five patches
2
```

```
% Extracting poles and zeros
omega = zeros(5,5) ;      % (patches, modes)
Omega = zeros(5,5) ;

for p = 1:5
    subsys = sys(p,p+5);
    list_poles = imag(pole(subsys));
    om = sort(list_poles(list_poles>=0));
    list_zeros = imag(zero(subsys));
    Om = sort(list_zeros(list_zeros>=0));
    for m = 1:5
        omega(p,m) = om(m);
        Omega(p,m) = Om(m);
    end
end

% Computing effective electromechanical coupling factor
Kji = zeros(5,5);
K_square_j_av = zeros(1,5);
for j = 1:5      % patches
    for i=1:5     % modes
        Kji(j,i) = sqrt((Omega(j,i)^2 - omega(j,i)^2)/(Omega(j,i)
            ^2));
        K_square_j_av(j) = K_square_j_av(j) + Kji(j,i)^2 ;
    end
end

%%% RL mean shunt

% Computing overall electromechanical coupling factor (only for 3
    patches)
K_overall = sqrt(K_square_j_av(1) + K_square_j_av(3) +
    K_square_j_av(5));

% C_static obtained at frequency 0
C_static = abs(evalfr(sys(1,6), 0)) ;
omega_mean = (1/5)*(omega(1,1) + omega(2,2) + omega(3,3) + omega
    (4,4) + omega(5,5)) ;

R = (2*K_overall)/(omega_mean*C_static);
L = 1/(C_static*(omega_mean^2));

RL = tf([L R 0],1);  % Ls^2 + Rs

% Implementation of the feedback
sys_shunted = feedback(sys, RL, 6, 1, 1);
sys_shunted = feedback(sys_shunted, RL, 8, 3, 1);
```

```
46 sys_shunted = feedback(sys_shunted, RL, 10, 5, 1);
47
48 % sys_shunted is the final system
```

D.4 Finding optimal RL shunt

The code generates the shunted state space model of the bladed rail from a five patches model, choosing the parameters with the H_∞ optimisation.

```
1  clc; clear all;
2
3  load('system_with_five_patches.mat') ;    % loading state space
       model with five patches
4
5  x0 = [1.1930e+03, 3.047];    % Initial conditions Mokrani
6
7  x = fminsearch(@Hinfty_oneRL_optimisation,x0)  % minimisation of
       Hinfty function
8
9  s = tf('s');
10 Z = x(1)*s + x(2)*(s^2);
11
12 sys_Rshunted1 = feedback(sys, Z, 6, 1, 1);
13 sys_Rshunted2 = feedback(sys_Rshunted1, Z, 7, 2, 1);
14 sys_Rshunted3 = feedback(sys_Rshunted2, Z, 8, 3, 1);
15 sys_Rshunted4 = feedback(sys_Rshunted3, Z, 9, 4, 1);
16 sys_Rshunted5 = feedback(sys_Rshunted4, Z, 10, 5, 1);
17 % gives the shunted system
18
19
20 function y = Hinfty_oneRL_optimisation(x)
21
22 load('system_with_five_patches.mat') ;    % loading state space
       model with five patches
23
24 s = tf('s');
25 vect = 6000:0.1:10300;  % % range of frequency in which peaks are
       computed
26 R = x(1);
27 L = x(2);
28 if x(1)>0 && x(2)>0  % Resistance must be positive
29     Z = R*s + L*(s^2);
30
31     % Implementing shunt
32     sys_Rshunted1 = feedback(sys, Z, 6, 1, 1);
33     sys_Rshunted2 = feedback(sys_Rshunted1, Z, 7, 2, 1);
34     sys_Rshunted3 = feedback(sys_Rshunted2, Z, 8, 3, 1);
35     sys_Rshunted4 = feedback(sys_Rshunted3, Z, 9, 4, 1);
```

```
36      sys_Rshunted5 = feedback(sys_Rshunted4, Z, 10, 5, 1);
37
38      % Obtaining Frequency Response Magnitude
39      [Mag1,Phase1,Wout1] = bode(sys_Rshunted5(6,1),vect);
40      [Mag2,Phase2,Wout2] = bode(sys_Rshunted5(7,2),vect);
41      [Mag3,Phase3,Wout3] = bode(sys_Rshunted5(8,3),vect);
42      [Mag4,Phase4,Wout4] = bode(sys_Rshunted5(9,4),vect);
43      [Mag5,Phase5,Wout5] = bode(sys_Rshunted5(10,5),vect);
44
45      % Obtaining the maximum of Freq. Resp. for each blade
46      y1 = max(abs(squeeze(Mag1)));
47      y2 = max(abs(squeeze(Mag2)));
48      y3 = max(abs(squeeze(Mag3)));
49      y4 = max(abs(squeeze(Mag4)));
50      y5 = max(abs(squeeze(Mag5)));
51      y_list = [y1, y2, y3, y4, y5];
52      y = max(y_list);
53  else
54      y = Inf;
55  end
56  end
```

D.5 Shunt mistuning sensibility

The code allows to plot the peak reduction when the electrical frequency of the RL shunt is changed.

```
1  clc; clear all;
2
3  load('system_with_five_patches.mat') ;    % loading state space
       model with five patches
4
5  vect = 6000:0.1:10300;     % range of frequency in which peak
       reduction is computed
6
7  R0 = 1193;          % shunt resistance (obtained for mean shunt)
8  L0 = 3.047;         % initial shunt inductance (obtained for mean
       shunt)
9  omega_av = 7.8120e+03;    % mean frequency
10 C = 1/(L0*(omega_av^2));
11 s = tf('s');
12 ratio = 0.9:0.001:1.1;  % mistuning ratio
13 dB_dy_list = zeros(size(ratio));
14 it = 0 ;
15 for r = ratio
16     it = it + 1;
17     mistuned_om = r*omega_av;     % new electrical frequency
```

```
18      L = 1/(C*(mistuned_om^2));    % inductance obtained from new
            electrical frequency
19      Z = R0*s + L*(s^2);
20      % creating the corresponding shunted system with feedbacks
21      sys_Rshunted1 = feedback(sys, Z, 6, 1, 1);
22      sys_Rshunted2 = feedback(sys_Rshunted1, 0, 7, 2, 1);
23      sys_Rshunted3 = feedback(sys_Rshunted2, Z, 8, 3, 1);
24      sys_Rshunted4 = feedback(sys_Rshunted3, 0, 9, 4, 1);
25      sys_Rshunted5 = feedback(sys_Rshunted4, Z, 10, 5, 1);
26
27      % extracting the magnitude of the original system for blades
            displacement
28      [Mag01,Phase01,Wout01] = bode(sys(6,1),vect);
29      [Mag02,Phase02,Wout02] = bode(sys(7,2),vect);
30      [Mag03,Phase03,Wout03] = bode(sys(8,3),vect);
31      [Mag04,Phase04,Wout04] = bode(sys(9,4),vect);
32      [Mag05,Phase05,Wout05] = bode(sys(10,5),vect);
33      y01 = max(abs(squeeze(Mag01)));
34      y02 = max(abs(squeeze(Mag02)));
35      y03 = max(abs(squeeze(Mag03)));
36      y04 = max(abs(squeeze(Mag04)));
37      y05 = max(abs(squeeze(Mag05)));
38
39      % extracting the magnitude of the shunted system for blades
            displacement
40      [Mag1,Phase1,Wout1] = bode(sys_Rshunted5(6,1),vect);
41      [Mag2,Phase2,Wout2] = bode(sys_Rshunted5(7,2),vect);
42      [Mag3,Phase3,Wout3] = bode(sys_Rshunted5(8,3),vect);
43      [Mag4,Phase4,Wout4] = bode(sys_Rshunted5(9,4),vect);
44      [Mag5,Phase5,Wout5] = bode(sys_Rshunted5(10,5),vect);
45      y1 = max(abs(squeeze(Mag1)));
46      y2 = max(abs(squeeze(Mag2)));
47      y3 = max(abs(squeeze(Mag3)));
48      y4 = max(abs(squeeze(Mag4)));
49      y5 = max(abs(squeeze(Mag5)));
50
51      % Computing the difference
52      dy_list = [dB(y1)-dB(y01), dB(y2)-dB(y02), dB(y3)-dB(y03), dB
            (y4)-dB(y04), dB(y5)-dB(y05)];
53
54      % Obtaining biggest peak reduction
55      dy = max(dy_list);
56      %dB_dy = 20*log10(dy);
57      dB_dy_list(it) = dy;
58  end
59
60  % plotting
```

```
fig6 = figure(6);
plot(ratio, dB_dy_list)
xlim([ratio(1) ratio(end)]);
xlabel('\omega_c /\omega_s','fontweight','bold')
ylabel('Maximum peak attenuation (dB)','fontweight','bold')
set(gca,'FontSize',15)
grid
set(fig6, 'Position', [100 100 800 400])
```

D.6 Optimal integral control

The code provides the best parameters for integral control with ten patches. The optimisation criteria can be H_∞ optimisation or damping maximisation.

```
clc; clear all;

x0 = 1.5527e+06;
x = fminsearch(@Hinfty_integrator,x0)      % Using H infinity
    optimisation
% OR: x = fminsearch(@MaxDamping_Integrator,x0)

s = tf('s');
I = x/s;    % integrator

load('system_with_10_patches.mat')

sys = sys_config2_Size2_Patch2_wTips_;

sys_I1 = feedback(sys, I, 6, 1, -1);
sys_I2 = feedback(sys_I1, I, 7, 2, -1);
sys_I3 = feedback(sys_I2, I, 8, 3, -1);
sys_I4 = feedback(sys_I3, I, 9, 4, -1);
sys_I5 = feedback(sys_I4, I, 10, 5, -1);

[GainMargin, PhaseMargin] = MIMO_margins(I,0.1);
% Gives the optimal controlled system and the corresponding
    margins

function y = Hinfty_integrator(x)

load('system_with_10_patches.mat')
sys = sys10;

s = tf('s');
vect = 7000:0.1:9000; % range of frequency in which peaks are
    computed
x
I = x/s;
```

```
sys_I1 = feedback(sys, I, 6, 1, -1);
sys_I2 = feedback(sys_I1, I, 7, 2, -1);
sys_I3 = feedback(sys_I2, I, 8, 3, -1);
sys_I4 = feedback(sys_I3, I, 9, 4, -1);
sys_I5 = feedback(sys_I4, I, 10, 5, -1);
if isstable(sys_I5)
    [Mag1,Phase1,Wout1] = bode(sys_I5(6,1),vect);
    [Mag2,Phase2,Wout2] = bode(sys_I5(7,2),vect);
    [Mag3,Phase3,Wout3] = bode(sys_I5(8,3),vect);
    [Mag4,Phase4,Wout4] = bode(sys_I5(9,4),vect);
    [Mag5,Phase5,Wout5] = bode(sys_I5(10,5),vect);
    y1 = max(abs(squeeze(Mag1)));
    y2 = max(abs(squeeze(Mag2)));
    y3 = max(abs(squeeze(Mag3)));
    y4 = max(abs(squeeze(Mag4)));
    y5 = max(abs(squeeze(Mag5)));
    y_list = [y1, y2, y3, y4, y5];
    y = max(y_list);
else
    y = Inf;
end


function y = MaxDamping_Integrator(x)

load('system_with_10_patches.mat')

s = tf('s');
vect = 6000:0.1:10300;
x ;
Gm_limit = -Inf;
Pm_limit = -Inf;
y_limit = -0.0015;
I = x/s;
sys_I1 = feedback(sys, I, 6, 6, -1);
sys_I2 = feedback(sys_I1, I, 7, 7, -1);
sys_I3 = feedback(sys_I2, I, 8, 8, -1);
sys_I4 = feedback(sys_I3, I, 9, 9, -1);
sys_I5 = feedback(sys_I4, I, 10, 10, -1);

if isstable(sys_I5)

    if Gm_limit<0 && Pm_limit <0
       Gm = 0 ; Pm = 0;
    else
        [Gm, Pm] = MIMO_margins(I,1.5);    % Checking for
            sufficient margins
```

```
78          Gm
79          Pm
80      end
81
82      if Gm<Gm_limit
83          y = Inf;
84      elseif Pm<Pm_limit
85          y = Inf;
86      else
87
88          [Freq,D,poles] = damp(sys_I5);
89          F1 = Freq(Freq<10300);
90          index = max(size(F1));
91          D= D(1:index);
92          y = -min(D)
93 %                 if y > y_limit
94 %                     y = Inf;
95 %                 end
96      end
97 else
98      y = Inf;
99 end
```

D.7 Optimal NPF control

The code provides the best parameters for NPF control with ten patches. The optimisation criteria can be H_∞ optimisation or damping maximisation.

```
1  clc; clear all;
2
3  x0 = [3e9,7.900e3, 0.1];
4
5  x = fminsearch(@Hinfty_NPF,x0)
6  % OR: x = fminsearch(@MaxDamping_NPF,x0)
7
8  s = tf('s');
9  NPF = x(1)/(s^2 + 2*x(3)*x(2)*s + x(2)^2);
10
11 load('system_with_10_patches.mat')
12
13 sys_P1 = feedback(sys, NPF, 6, 6, -1);  % Closing the loop
       between Vsi and Vai
14 sys_P2 = feedback(sys_P1, NPF, 7, 7, -1);
15 sys_P3 = feedback(sys_P2, NPF, 8, 8, -1);
16 sys_P4 = feedback(sys_P3, NPF, 9, 9, -1);
17 sys_P5 = feedback(sys_P4, NPF, 10, 10, -1);
18
19 [GainMargin, PhaseMargin] = MIMO_margins(NPF,0.1);
```

```
20
21 % Gives the optimal controlled system and the corresponding
       margins
22
23
24
25 function y = Hinfty_NPF(x)
26
27 load('system_with_10_patches.mat')
28
29 s = tf('s');
30 vect = 7000:0.1:10000;
31 Gm_limit = -Inf;
32 Pm_limit = -Inf;
33
34 NPF = x(1)/(s^2 + 2*x(3)*x(2)*s + x(2)^2);
35
36 if x(3) <1     % Must be smaller than 1
37
38     sys_P1 = feedback(sys, NPF, 6, 6, -1);    % Closing the loop
           between Vsi and Vai
39     sys_P2 = feedback(sys_P1, NPF, 7, 6, -1);
40     sys_P3 = feedback(sys_P2, NPF, 8, 6, -1);
41     sys_P4 = feedback(sys_P3, NPF, 9, 9, -1);
42     sys_P5 = feedback(sys_P4, NPF, 10, 10, -1);
43     if isstable(sys_P5)
44         if Gm_limit<0 && Pm_limit <0
45            Gm = 0 ; Pm = 0;
46         else
47             [Gm, Pm] = MIMO_margins(NPF,1.5)      % Checking if
                   stability margins are sufficient
48         end
49
50         if Gm<Gm_limit
51             y = Inf;
52         elseif Pm<Pm_limit
53             y = Inf;
54         else
55
56             [Mag1,Phase1,Wout1] = bode(sys_P5(1,1),vect);
57             [Mag2,Phase2,Wout2] = bode(sys_P5(2,2),vect);
58             [Mag3,Phase3,Wout3] = bode(sys_P5(3,3),vect);
59             [Mag4,Phase4,Wout4] = bode(sys_P5(4,4),vect);
60             [Mag5,Phase5,Wout5] = bode(sys_P5(5,5),vect);
61             y1 = max(abs(squeeze(Mag1)));
62             y2 = max(abs(squeeze(Mag2)));
63             y3 = max(abs(squeeze(Mag3)));
```

```
64              y4 = max(abs(squeeze(Mag4)));
65              y5 = max(abs(squeeze(Mag5)));
66              y_list = [y1, y2, y3, y4, y5];
67              y = max(y_list);
68          end
69      else
70          y = Inf;
71      end
72  else
73      y = Inf;
74  end
75
76  function y = MaxDamping_NPF(x)
77
78  load('system_with_10_patches.mat')
79
80  s = tf('s');
81  vect = 6000:0.1:10300;
82  x ;
83  Gm_limit = 10;
84  Pm_limit = 15;
85  y_limit = -0.0015;
86  NPF = x(1)/(s^2 + 2*x(3)*x(2)*s + x(2)^2);
87  if x(3) <1
88
89      sys_P1 = feedback(sys, NPF, 6, 6, -1);     % Closing the loop
            between Vsi and Vai
90      sys_P2 = feedback(sys_P1, NPF, 7, 7, -1);
91      sys_P3 = feedback(sys_P2, NPF, 8, 8, -1);
92      sys_P4 = feedback(sys_P3, NPF, 9, 9, -1);
93      sys_P5 = feedback(sys_P4, NPF, 10, 10, -1);
94      if isstable(sys_P5)
95
96          if Gm_limit<0 && Pm_limit <0
97              Gm = 0 ; Pm = 0;
98          else
99              [Gm, Pm] = MIMO_margins(NPF,1.5);
100             Gm
101             Pm
102         end
103
104         if Gm<Gm_limit
105             y = Inf;
106         elseif Pm<Pm_limit
107             y = Inf;
108         else
109
```

```
110                 [Freq,D,poles] = damp(sys_P5);      % Computes damping
111                 F1 = Freq(Freq<10300);
112                 index = max(size(F1));
113                 D= D(1:index);
114                 y = -min(D)
115 %                   if y > y_limit
116 %                       y = Inf;
117 %                   end
118             end
119         else
120             y = Inf;
121         end
122 else
123         y = Inf;
124 end
```

D.8 MIMO Margins

The code computes the stability margins of the controller for a MIMO system as explained in Chapter 4.

```
1  function [gain_m, phase_m] = MIMO_margins(controller, d)
2
3  C=controller;    % integrator or NPF
4
5  load('system_with_10_patches.mat')
6
7  sys_C1 = feedback(sys, C, 6, 6, -1);  % Closing the loop between
       Vai and Vsi
8  sys_C2 = feedback(sys_C1, C, 7, 7, -1);
9  sys_C3 = feedback(sys_C2, C, 8, 8, -1);
10 sys_C4 = feedback(sys_C3, C, 9, 9, -1);
11 sys_C5 = feedback(sys_C4, C, 10, 10, -1);
12
13 if not(isstable(sys_C5))
14     gain_m = 0; phase_m = 0;
15     return
16 end
17
18 % Gain margin
19
20 gain_m = -1;
21
22 for dB = 0:1*d:500      % Testing gain increment of between 0 and
       500 dB
23     dB;
24     g = 10^(dB/20);
25     Cg = g*C;           % Changing controller's gain
```

```
26      sys_C1 = feedback(sys, Cg, 6, 6, -1);
27      sys_C2 = feedback(sys_C1, Cg, 7, 7, -1);
28      sys_C3 = feedback(sys_C2, Cg, 8, 8, -1);
29      sys_C4 = feedback(sys_C3, Cg, 9, 9, -1);
30      sys_C5 = feedback(sys_C4, Cg, 10, 10, -1);
31
32      stable = isstable(sys_C5);
33      if not(stable)
34          gain_m = dB;
35          break
36      end
37
38  end
39
40  if gain_m == -1
41      gain_m = Inf;
42  end
43
44  % Phase margin
45  phase_m1 = 0;
46  for phase = 0:0.5*d:180             % Testing gain increment of
        between 0 and 180 degrees
47      phase;
48      Cp1 = exp(pi*(phase/180)*1i)*C;      % Changing controller's
            phase
49      sys_C1 = feedback(sys, Cp1, 6, 6, -1);
50      sys_C2 = feedback(sys_C1, Cp1, 7, 7, -1);
51      sys_C3 = feedback(sys_C2, Cp1, 8, 8, -1);
52      sys_C4 = feedback(sys_C3, Cp1, 9, 9, -1);
53      sys_C5 = feedback(sys_C4, Cp1, 10, 10, -1);
54
55      stable = isstable(sys_C5);
56      if not(stable)
57          phase_m1 = phase;
58          break
59      end
60
61
62  end
63
64
65  phase_m2 = 0;
66  for phase = 0:-0.5*d:-180
67      phase;
68      Cp2 = exp(pi*(phase/180)*1i)*C;
69      sys_C1 = feedback(sys, Cp2, 6, 6, -1);
70      sys_C2 = feedback(sys_C1, Cp2, 7, 7, -1);
```

```
71      sys_C3 = feedback(sys_C2, Cp2, 8, 8, -1);
72      sys_C4 = feedback(sys_C3, Cp2, 9, 9, -1);
73      sys_C5 = feedback(sys_C4, Cp2, 10, 10, -1);
74
75      stable = isstable(sys_C5);
76      if not(stable)
77          phase_m2 = phase;
78          break
79      end
80 end
81 phase_margins = [phase_m1 abs(phase_m2)];
82 phase_m = min(phase_margins) ;
```

D.9 Fitting the experimental curve with a model

The code creates a model to fit experimental data.

```
1
2 % Defining fitting model parameters
3 a0= 1.5; a1 = 1.5; a2 = 0.4; a3=0.3; a4=0.45;  a5=0.25;
4 a6 = 1; a7 = 0.3; a8=0.4; a9=0.45;  a10=5;
5 y = [a1*0.001137515838961,a2*0.001249877212735,a3
      *0.001163909473054,a4*0.001167887670335,a5*0.001167887670335];
6 z = [a6*0.001137515838961,a7*0.001249877212735,a8
      *0.001163909473054,a9*0.001167887670335,a10
      *0.001167887670335];
7 G0 = a0*1e-3;
8
9 %%%% Data reading
10 load exp2_047.mat
11 syst=exp2_047;
12 n = syst.Y(1).Data;
13 s = syst.Y(3).Data;
14 t=syst.X.Data;
15 dt=t(2)-t(1);
16 ff=1/dt;
17 dd=2^16;
18 han=hanning(dd);
19
20
21 [Txf,Fr] = tfestimate(n,s,han,[],dd,ff);
22 aTxf = abs(Txf);
23 % plot(Fr, aTxf);
24 radFr = 2*pi*Fr;
25 s_fr = size(radFr);
26 ind_in = 0 ; ind_fin = 0;
27 for j=1:s_fr(1)
28      if ind_in == 0;
```

```
29          if radFr(j)>= 7000
30              ind_in = j;
31          end
32      end
33      if ind_fin == 0;
34          if radFr(j)>= 8700;
35              ind_fin = j;
36          end
37      end
38  end
39
40  radFr = radFr(ind_in:ind_fin);
41  aTxf = aTxf(ind_in:ind_fin);
42  shortTxf = Txf(ind_in:ind_fin);
43
44  %%%% Model
45
46  % Poles pi and zeros zi for experimental data
47  p1 = 2*pi*1271.17770513;
48  p2 = 2*pi*1286.06304568;
49  p3 = 2*pi*1291.98680366;
50  p4 = 2*pi*1296.23975810;
51  p5 = 2*pi*1300.64460378;
52  z1 = 2*pi*1273.60796481;
53  z2 = 2*pi* 1290.16410890;
54  z3 = 2*pi*1293.50571596;
55  z4 = 2*pi*1296.54354056;
56  z5 = 2*pi*1355.02166417;
57
58  % Computation of numerators and denominators for the transfer
        function
59  D1 = tf([1 (2*p1)*y(1) (p1^2)],1);
60  D2 = tf([1 (2*p2)*y(2) (p2^2)],1);
61  D3 = tf([1 (2*p3)*y(3) (p3^2)],1);
62  D4 = tf([1 (2*p4)*y(4) (p4^2)],1);
63  D5 = tf([1 (2*p5)*y(5) (p5^2)],1);
64
65  N1 = tf([1 (2*z1)*z(1) (z1^2)],1);
66  N2 = tf([1 (2*z2)*z(2) (z2^2)],1);
67  N3 = tf([1 (2*z3)*z(3) (z3^2)],1);
68  N4 = tf([1 (2*z4)*z(4) (z4^2)],1);
69  N5 = tf([1 (2*z5)*z(5) (z5^2)],1);
70
71  %Transfer function fitting the experimental curve
72  G = 1i*G0*(N1*N2*N3*N4*N5)/(D1*D2*D3*D4*D5);
73
74
```

```
%Plotting

a = bode(G, radFr);
s = size(radFr);
b = zeros(size(s));
for i = 1:s(1)
    b(i) = a(1,1,i) ;
end
figure(2); loglog(radFr, aTxf, 'b')
hold on;
loglog(radFr, b,'r')
legend('Experimental data', 'Model')
xlabel('Frequency (rad/s)')
ylabel('Magnitude')

figure(3);
plot(radFr, angle(shortTxf)/pi*180, 'b')
[Mag,Phase,Wout] = bode(G,radFr);
hold on; plot(radFr,squeeze(Phase),'r');
legend('Experimental data', 'Model')
xlabel('Frequency (rad/s)')
ylabel('Phase (Degrees)')
```